

# Compaction effects on evaporation and salt precipitation in drying porous media

Nurit Goldberg-Yehuda <sup>1,2</sup>, Shmuel Assouline <sup>1</sup>, Yair Mau <sup>2</sup>, Uri Nachshon <sup>1</sup>

<sup>1</sup>Institute of Soil, Water and Environmental Sciences, Agricultural Research Organization-Volcani Institute,  
Rishon Lezion 7505101, Israel

<sup>2</sup>The Institute of Environmental Sciences, The Robert H. Smith Faculty of Agriculture, Food and Environment, The Hebrew University of Jerusalem, Rehovot 7610001, Israel

Correspondence to: Uri Nachshon (urina@agri.gov.il)

## Abstract

Compaction and salinization of soils reduce croplands fertility, affect natural ecosystems, and are major concerns worldwide. Soil compaction alters soil structure and affects the soil's hydraulic properties, and it therefore may have a significant impact on evaporation and solute transport processes in the soil. In this work, we investigated the combined processes of soil compaction, bare soil evaporation, and salt precipitation. X-ray computed micro tomography techniques were used to study the geometrical soil pore and grain parameters influenced by compaction. The impact of compaction on evaporation and salt precipitation was studied using column experiments. We found that compaction reduced the average grain size and increased the number of grains, due to the crushing of the grains and their translocation within the compacted soil profile. Changes in pore and grain geometry and size were heterogeneously distributed throughout the soil profile, with changes most apparent near the source of compaction, in our case, at the soil surface. The column experiments showed that the presence of small pores in the upper layer of the compacted soil profile leads to higher evaporation loss and salt precipitation rates, due to the increase of hydraulic connectivity to the soil surface and the prolongation of the first stage of evaporation.

30           **1. Introduction**

Soil compaction is a major cause of soil degradation in agricultural environments (Akker and Canarache, 2001; Hamza and Anderson, 2005; Pagliai et al., 2003). It is associated with the increase of soil bulk density and decrease of porosity (Mossadeghi-Björklund et al., 2016). Soil compaction at different intensities may occur due to natural processes such as the impact of  
35    raindrops, natural soil-forming processes, animal treading, and to processes linked to human activities, especially in agricultural environments, such as intense vehicular traffic over the fields (Assouline, 2004; Pagliai et al., 2003; Shah et al., 2017; Mossadeghi-Björklund et al., 2018). Passing of heavy machinery and vehicles over the fields leads to compaction as a result of pure static stresses, wheel slip and dynamic forces, caused by vibration of the engine and  
40    the attached implements (Horn et al., 1995). Barik et al. (2014) found significant variability in the spatial distribution of the aggregate stability, bulk density, total porosity, penetration resistance, and moisture content values, following traffic operation over arable lands. Pores nearby the location of compression are strongly affected, whereas those located further away from the source of compaction are less affected (Keller et al., 2019; Schlüter and Vogel, 2016).  
45    Thus, compaction resulting from traffic generally presents a sigmoidal distribution with depth of the soil bulk density, where the denser part is close to the surface (Assouline, 2004; Augeard et al., 2007; Bresson et al., 2004; Dejong-Hughes et al., 2001; Horton et al., 1994; Reicosky et al., 1981).

To overcome soil compaction in arable lands and to loosen up the soil upper layer, soil tillage  
50    is implemented, producing favorable conditions for seed germination and crop root development. Soil tillage reduces soil bulk density, increases porosity, homogenizes soil-wetting processes and improves soil aeration in the root zone (de Almeida et al., 2018; Assouline et al., 2014; Rasmussen, 1999; El Titi, 2003). On the other hand, under certain

conditions, tillage may accelerate processes of soil erosion and compaction of the soil at the  
55 lower boundary of the tilled zone (de Almeida et al., 2018), i.e., the plough pan (Podder et al.,  
2012). Therefore, minimizing vehicle passing over the fields, reducing tillage, and improving  
our understanding of the nature of soil compaction is important.

### **1.1. Soil compaction at the micro-scale**

At the microscale, stresses in soil do not propagate homogeneously but rather through  
60 preferential paths – in all directions (Nawaz et al., 2013). Consequently, soil deformation  
occurs at specific sites, where the stresses and strains are maximal. These areas, known also  
as shear bands, are those that undergo structural deformation, while soil volumes in between  
the stress chains may preserve their original structure and porosity (Nawaz et al., 2013;  
Naveed et al., 2016). The heterogeneous effect of compaction on the physical properties of  
65 the soil leads to an uneven spatial distribution of the soil's hydraulic properties that in turn  
affect water flow and solute transport processes in the soil profile (Alaoui et al., 2018;  
Assouline, 2006a, 2006b; Assouline and Or, 2006).

Soil compaction affects the pore network in the soil profile, with respect to: (i) pore-size  
distribution; (ii) pore geometry and morphology; and (iii) pore connectivity (Horn et al., 1995;  
70 Mossadeghi-Björklund et al., 2016). Consequently, water-related soil properties are  
significantly altered (Horn et al., 1995; Assouline, 2006a; b). These changes affect unsaturated  
soil hydraulic properties and reduce saturated soil hydraulic conductivity, thus increasing  
surface runoff and soil erosion by water (Alaoui et al., 2011; Keller et al., 2013; Shah et al.,  
2017; Soane and van Ouwerkerk, 1995). In addition, soil aeration is reduced and the  
75 heterogeneous changes of the soil's physical and hydrological properties, may lead to the  
formation of preferential water flow paths in the soil (Alaoui et al., 2011; Keller et al., 2013;  
Soane and van Ouwerkerk, 1995). Consequently, solute transport and accumulation in the soil  
may be affected, impacting nutrient availability to plants (Horn et al., 1995; Lipiec and

Stępniewski , 1995; Hendrickx and Flury, 2001; Mossadeghi-Björklund et al., 2016). The  
80 above-mentioned changes of the soil properties, due to compaction, usually occur at the top  
30 cm of the soil profile (Horn et al., 1995; Keller et al., 2019). These changes in the soil  
structure of the upper soil layer have impacts on the soil water balance in general, and on  
infiltration and evaporation processes in particular (Assouline et al., 2007, 2014; Shokri et al.,  
2010; Sillon et al., 2003).

## 85 **1.2. Bare soil evaporation**

Evaporation plays a central role in the hydrologic cycle and surface energy balance (Bergstad  
et al., 2018) as it is the main process of soil-water transfer to the atmosphere (Brutsaert, 2005;  
Hillel, 1980). The evaporation in porous media is affected by and involves complex and highly  
dynamic interactions between boundary conditions, liquid flow and vapor diffusion (Lehmann  
90 et al., 2008; Or et al., 2013; Assouline et al., 2014; Kamai and Assouline, 2018; Assouline and  
Kamai, 2019).

The evaporation process from bare soils consists of two stages: stage 1 (S1) and stage 2 (S2).  
Evaporation during S1 takes place at the soil surface, and a hydraulic connection is maintained  
throughout the soil profile, by capillary flow of water through the soil's small pores (Lehmann  
95 et al., 2008; Nachshon et al., 2011a; b; Bergstad et al., 2018; Assouline and Narkis, 2019). In  
parallel to the upward capillary flow, through the small pores, the larger pores in the soil are  
air invaded. The interface between saturated and partially dry regions is defined as the drying  
front (Shokri et al., 2008). S1 is characterized by a high and relatively constant evaporation  
rate affected by soil properties and atmospheric conditions (Hillel, 1980). S2 begins when a  
100 characteristic capillary head,  $\psi_c$ , is reached at the soil surface, thus the small pores are air  
invaded, and the hydraulic connection between the soil profile and the surface is lost (Prat,  
2002; Lehmann et al., 2008; Assouline et al., 2014). The evaporation front, that is the upper  
boundary of the capillary rise through the small pores (Shokri et al., 2008), migrates

downward, and evaporation rate is drastically reduced as vapor diffusion from the  
105 evaporation front to the atmosphere governs the process (Lehmann et al., 2008; Nachshon et  
al., 2011b; Or et al., 2013; Kamai and Assouline, 2018).

Over recent years, several works have shown that soil structure has a strong effect on bare  
soil evaporation. Lehmann et al. (2008), and following works (e.g., Lehmann and Or, 2009;  
Nachshon et al., 2011a, b) have shown that heterogeneous structure of the porous media,  
110 consisting of two texturally different matrices (coarse and fine) separated by a sharp interface  
perpendicular to the evaporation front, results in elongation of S1 and increased cumulative  
evaporation. In short, this is a result of the large pores of the coarse media that are being  
invaded by air much before the fine pores, with the lower (more negative) air entry pressure.  
The pressure head differences between the large and fine pores results in that the coarse  
115 texture domain supplies water, by capillary flow, to the fine texture domain, thus more water  
is available for S1, through the fine pores (Lehmann and Or, 2009).

In addition, structural changes of the soil along the vertical axis (with depth), may also affect  
evaporation (e.g., Or et al., 2007; Lehmann et al., 2008; Shokri et al, 2010; Assouline et al.,  
2014; Assouline and Narkis, 2019). It was shown that porous media composed of a fine texture  
120 domain that overlies a coarse texture domain may result in longer duration of S1 and  
increased cumulative evaporation with respect to the homogeneous domain, composed of  
the coarse texture matrix only. In the layered structure, as soon as the drying front reaches  
the layers with the relatively larger pores, rapid water displacement will occur from the large  
pores to the overlying finer pores. The pressure in the coarse layer changes abruptly from its  
125 air-entry value to the air-entry value at the evaporation front, which is associated to the higher  
capillary suction of the small pores (Or et al, 2007; Shokri et al, 2010). Consequently, the  
coarse texture layer acts as a water reservoir that supplies extra water to sustain a longer S1  
and higher cumulative evaporation, compared to the homogeneous soil structure. It is

important to emphasize that this process will occur only if the thickness of the fine texture  
130 layer is shorter than its characteristic length as only at this state the drying front may reach  
the coarse texture domain, while the system is at S1 and the evaporation front is still at the  
soil surface (Assouline et al., 2014; Assouline and Narkis, 2019).

### **1.3. Evaporation and soil salinization**

Evaporation and soil salinization are tightly connected processes, especially in cultivated  
135 fields. Soil salinization in cultivated fields is a common feature resulting from low-quality  
irrigation water, fertilization, and saline and shallow groundwater resulting from inadequate  
irrigation and drainage practices (Yakirevich et al., 2013; Berezniak et al., 2018; Nachshon,  
2018; Hopmans et al., 2021).

The presence of salts in the soil pore water reduces the osmotic potential of the solution and  
140 the equilibrium water vapor pressure (Nassar and Horton, 1997). Consequently, evaporation  
rates from a saline soil are expected to be lower compared to solute-free conditions. During  
evaporation, the concentration of the dissolved ions increases in the pore solution, until  
saturation is reached and salt precipitation begins (Nachshon et al., 2011a). Salt precipitation  
at the soil surface occurs mainly during S1, where the evaporation rate is maximal and solutes  
145 are continuously transported to the evaporation front at the soil surface by capillary flow. As  
the salt begins to precipitate and expands over the soil surface, the evaporation rate is  
affected by the pore-scale dynamics of the precipitated salt (Bergstad et al., 2017, 2018), and  
the consequent changes to liquid and vapor flow processes through the salt crust. The  
presence of porous media heterogeneities (Lehmann and Or, 2009; Nachshon et al., 2011a),  
150 initial solute concentration of the pore water (Rad and Shokri, 2012; Shokri-Kuehni et al.,  
2017), soil surface properties (Nachshon et al., 2011b) and salt type (Shokri-Kuehni et al.,  
2017) may affect the dynamics of the salt precipitation layer and its influence on evaporation  
(Bergstad et al., 2018). In some cases, if the precipitated salt layer over the soil surface is

hydraulically connected to the solution in the pores below, it may accelerate evaporation, as  
155 the surface area of the precipitated salt is usually higher compared to the underlying bare soil.  
Consequently, as long as the salt crust can pump liquid water from the underlying media, the  
elevated surface area of the salt crust would increase total evaporation (Shokri-Kuehni et al.,  
2017). In addition, roughness changes of the matrix-atmosphere interface by the precipitated  
salt crust may also increase evaporation due to changes of wind speed and surface energy  
160 balance (Kampf et al., 2005; Nield et al., 2015). On the other hand, if the precipitated salt layer  
is hydraulically disconnected from the solution in the pores, it acts as a barrier that reduces  
vapor diffusion from the soil to the atmosphere, and cumulative evaporation and evaporation  
rates will be reduced (Nachshon et al., 2011a).

Previous studies have shown that changes in soil structure, which affect evaporation,  
165 influence also the nature and location of salt precipitation in the presence of saline solution  
(Bergstad et al., 2017; Nachshon et al., 2011a, 2011b). The drying patterns and dynamics are  
greatly influenced by the presence of textural discontinuities that may result in preferential  
drying and promotion of capillary exchange between different regions in the soil (Bergstad et  
al., 2017; Lehmann and Or, 2009). As aforementioned, soil compaction affects soil structural  
170 and textural properties, mainly at the soil surface, where evaporation and salt precipitation  
are prominent.

#### **1.4. Evaporation and soil compaction**

Studies on the effect of soil compaction on evaporation, in general, and its relation to salt  
precipitation in particular, are scarce. Nassar and Horton (1999) examined salinity and  
175 compaction effects on soil water evaporation from bare soils, focusing on water and solute  
distributions in the soil. They showed that compaction increases cumulative evaporation, due  
to increased matric suction of the compacted soil, resulting in the increase of the soil water  
holding capacity and unsaturated hydraulic conductivity. Consequently, water flows more

efficiently from deep parts of the soil profile to the soil surface, where evaporation is maximal,  
180 at S1 evaporation. In their study, Nassar and Horton (1999) deliberately compacted the soil  
samples in a homogeneous manner, ignoring the heterogeneous nature of soil compaction.  
Moreover, while the authors examined the impact of compaction and evaporation on solute  
distribution in the soil profile, and its impact on the solution osmotic potential, they did not  
consider the interactions between soil compaction, evaporation, and salt precipitation.

185 Sillon et al. (2003), using indirect measurements under non-saline field conditions, also  
pointed at higher evaporation from compacted soils. The authors showed that for compacted  
soils, soil drying occurred from bottom to top, as opposed to regular evaporative conditions,  
where the drying front recedes from the surface downward. In agreement with Nassar and  
Horton (1999), this was explained by the high capillary suction of the compacted soil that  
190 enabled pumping of water from the lower parts of the soil profile to the soil surface, where  
evaporation takes place. Assouline and Narkis (2019) used a constructed multilayered porous  
medium, where the top layer had the highest bulk density, smallest grains, and smallest pores,  
and where the bulk density gradually decreased, while grains and pore sizes gradually  
increased in the underlying layers. They measured evaporation from this structure and from  
195 a structure where the order of the layers was reversed. It was shown that in the soil structure  
where the top layer had the highest bulk density the S1 duration was extended and the  
cumulative evaporation increased in comparison to the reversed structure. The concept of the  
characteristic length was applied to explain these results, providing a physically-based support  
to the observations of Sillon et al. (2003).

200 The main objective of the work presented herein is to understand the impact of soil  
compaction on soil evaporation, solute distribution and salt precipitation, and their  
interactions, along the soil profile. Relying on previous works (Assouline and Narkis, 2019;  
Nassar and Horton, 1999; Sillon et al., 2003), we conducted a series of experiments to fill up



the knowledge gaps regarding the complex interactions between the heterogeneous  
205 structural nature of compacted soils, evaporation, and salt dynamics.

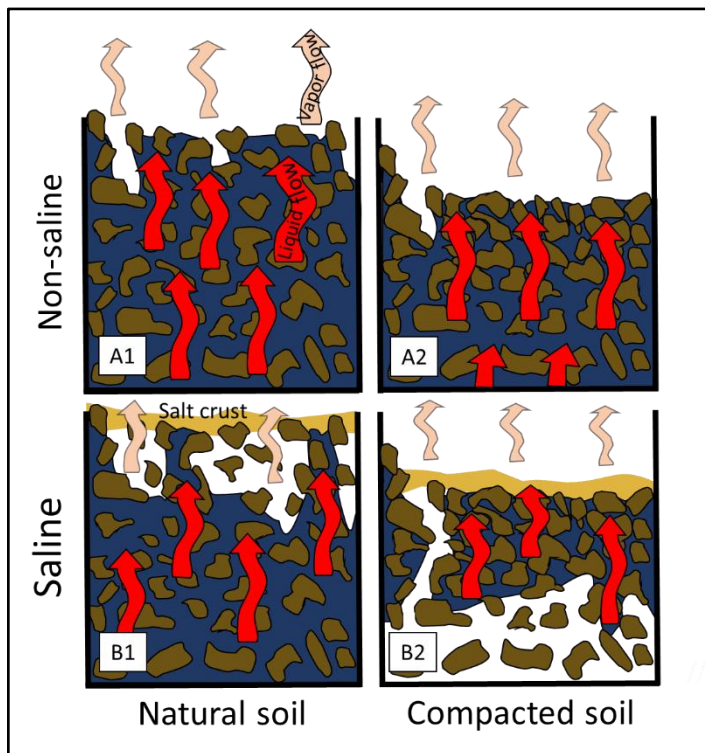
## 2. Conceptual model

Based on the studies detailed above, we hypothesize that compacted soil may be considered  
as a semi-layered structure where pore openings are minimal at the soil surface, due to  
compaction, and gradually increase with depth (**Figure 1A**). Consequently, soil bulk density,  
210 capillary suction, water holding capacity and unsaturated hydraulic conductivity are maximal  
at the upper layer of the soil profile, as well as its characteristic capillary length. These  
structural changes will result in evaporation patterns similar to those observed for the layered  
structure domain where fine media overlies a coarser texture domain.

It is hypothesized that for compacted conditions the first tip of the drying front that will invade  
215 the underlying larger pores, acting as an air conduit that will allow air to replace the water  
that will be pumped upward by the fine texture horizons (**Figure 1B(2)**). Consequently, at the  
compacted soil scenario, during evaporation, the upper layers of the medium will retain high  
levels of saturation, while the matrix will be dried from bottom to top. This will lead to higher  
cumulative evaporation and longer S1 duration, compared to the non-compacted state.

220 Under saline conditions, where the pores are filled with a salty solution, evaporation will lead  
to solute precipitation at the soil surface, and to the formation of an efflorescence salt crust,  
at least in the case of NaCl (Nachshon and Weisbrod, 2015; Piotrowski et al., 2020). Under  
non-compacted conditions, the receding drying front during evaporation and the resulted  
increased matric potential and reduction of the soil water content near the soil surface, will  
225 result in a quick transition into a state of a hydraulic discontinuity between the soil and the  
salt crust. Therefore, the salt crust will reduce evaporation as it acts as a barrier for water  
vapor diffusion from the evaporation front to the atmosphere (**Figure 1B(1)**). On the other  
hand, under the compacted soil condition, it is hypothesized that the drying pattern from

bottom to top and the high water saturation that is sustained near the soil surface, will  
 230 maintain a hydraulic connection between the soil profile and the upper surface of the salt  
 crust, which is now the active evaporation front of the system (**Figure 1B(2)**). Therefore, it is  
 hypothesized that even though more salt is expected to accumulate on the surface of the  
 compacted soil, due to the higher evaporation, its impact on evaporation will be moderate  
 compared to homogeneous non-compacted conditions.



235 **Figure 1: Conceptual model of evaporation and salt precipitation under compacted and non-**  
**compacted conditions; (A) initial stages of S1 evaporation with the first air invasion into the**  
**matrix. (B) advanced stages of evaporation, where most of the soil is hydraulically**  
 240 **disconnected from the salt crust for the non-compacted state (B1), whereas at the**  
**compacted state, most of the soil is hydraulically connected to the salt crust, thus**  
**evaporation front is at the salt crust upper surface (B2). Drying of the compacted media is**  
**from bottom to top, as liquid water is replaced by air that is flowing downward through the**  
**larger pores that act as air conduits.**

These hypotheses were tested herein by means of high-resolution micro CT scans, to  
 245 characterize, at the micro scale, the impact of compaction on soil pores and grains properties,  
 and column experiments to study the impact of compaction, at the macro-scale, on  
 evaporation and salt precipitation. A simple numerical model was used also, to strengthen  
 some aspects of the experimental findings and research hypotheses.

### 3. Materials and method

250 This study relies on three parts: (i) studying the impact of compaction on soil physical properties at the micro and macro scales; (ii) simple numerical simulation of evaporation from different soil structures, mimicking compacted and non-compacted conditions, with and without the presence of a precipitated salt crust; and (iii) validation of the conceptual model presented in **Figure 1** by means of macro scale evaporation experiments.

#### 255 **3.1. Micro scale changes of pores and grains physical properties due to compaction**

Imaging of sand samples before and after compaction was conducted in a non-destructive manner using a high-resolution  $\mu$ CT (SKYSCAN 1172, Bruker, Kontich, Belgium), in order to observe the impact of compaction on the sand physical structure, pores and grains dimensions, and spatial arrangement. The X-ray source voltage was 80 kV, and the electrical  
260 current, 10 mAs. The scan was done with aluminum and copper filters, with image rotation of  $0.2^\circ$ . Images with voxel resolution of  $4.42 \mu\text{m}$  were reconstructed by the software 'NRecon' (Bruker, Kontich, Belgium). Image analyses were carried out using designated MATLAB codes, the software 'CT-vox' (Bruker, Kontich, Belgium) and the open source image analysis software, ImageJ (Collins, 2007).

265 Polyvinyl chloride (PVC) tubes, 3-cm-long and 1.6-cm in diameter, open at the top and sealed at the bottom, were filled with quarry coarse sand (quartz), with mean grain diameter of  $\sim 500 \mu\text{m}$  (sand characteristics can be found in Nachshon, 2016). The columns were scanned before and following mechanical compaction, in order to detect the impact of compaction on  
270 microscale changes of the sand properties, as a function of depth and distance from the source of compression. Compaction was achieved using a PVC shaft that fits exactly the inner diameter of the column. The shaft was slowly pushed downward to compress the sand samples, using a hand-operated press, achieving a one-dimensional confined compression.

The samples were compressed down to a decrease of the total length of the sand sample by 2 mm, corresponding to an increase of ~7% of the packing bulk density of the samples.

275 The images from the  $\mu$ CT scans were used to analyze grain and pore sizes at the top 7 mm of the sand samples and at depth of 9-18 mm. Hereafter, the top and lower levels of the compacted samples will be referred to as 'TC' and 'LC', respectively, and the non-compacted control will be referred to as 'UN'. The TC and LC results were used to compare the impact of compaction at the top and the lower layers of the sample. Each  $\mu$ CT scan generates hundreds  
280 of images of 2D slices of the sample, with a 4.42  $\mu$ m distance between adjacent slices. For each scan, five 2D images, out of the hundreds of images, were chosen randomly, processed, and analyzed by a MATLAB code.

Grayscale calculations were based on Otsu's method, which selects the threshold to minimize the interclass variance (Otsu, 1979). Morphological operations were done to clean image  
285 noises. Grain counting and grain area calculations were done using the function '*regionprops*', at the MATLAB - Image Processing Toolbox. A distance heat map was generated using the Euclidean distance transform, '*bwdist*' and the function '*bwske*', both from the MATLAB - Image Processing Toolbox. Pore sizes were obtained by calculating the average maximal pore distance from the closest grain edge along the pores and throats. Grain distribution map was  
290 generated by counting the center of each grain. Size based segmentation and visualization of the sand grains was done using the 'Analyze Particles' function in ImageJ.

### **3.2. Macro scale changes at the soil profile due to compaction**

While the  $\mu$ CT experiments described above were used to study the effect of compaction at the pore scale, a transparent 10 cm long and 5 cm in diameter PVC column was used to  
295 examine the effect of compaction at the macro scale. The same coarse sand as detailed above was used in this experiment. To allow visual observation of changes in the compacted sand

column, 10% of the sand (by weight) was colored with a standard red spray paint. The colored sand was thoroughly mixed with the regular sand, before packing the column.

As described previously, the sand in the column was compacted by decreasing the total length  
300 of the sand sample by 5 mm, using a uniform hammer beating on a circular shaft, with the same diameter as the inner diameter of the PVC column. The bulk density of the sand sample was increased by ~5% following compaction.

Pictures of the sand column profile were taken before and after compaction by a single lens reflex camera (Canon - EOS60D, Japan), with an EFS18-200 mm lens (Canon, Japan).  
305 Compaction was evaluated by visual analysis of the images that captured the movement of the colored sand grains and measuring the translocation of the same colored grains before and after compaction.

### **3.3. Numerical model**

A preliminary analysis was carried out based on simulations using HYDRUS-1D (Šimůnek et al., 2013), in order to estimate the general impact of soil compaction on evaporation, with  
310 and without the presence of a precipitated salt crust. Four modeled setups were considered: (i) Homogeneous coarse texture domain, mimicking natural sandy soil with no compaction. Hereon this will be referred to as HC (Homo-Coarse); (ii) Homogeneous coarse texture domain that underlies a thin layer of a fine texture domain (1 cm), mimicking compaction of  
315 the very top layer of the soil profile. Hereon this structure will be referred to as HCC (Homo-Coarse-Compacted); (iii) Layered structure domain, which mimics a compacted soil where the effect of compaction is gradually decreased with depth. This modeled domain is composed of five discrete layers, 2 cm each, where the most upper layer had the smallest grain diameter, lowest saturated hydraulic conductivity and highest air entry pressure.  
320 Underlying layers were gradually comprised of bigger particles, higher hydraulic conductivity and lower air entry pressure. Hereon this layered structure with the fine texture matrix at its

upper levels will be referred to as FU (Fine-Up); and (iv) Homogeneous domain, composed of a homogeneous mixture of the particles that used to build the discrete layers of the layered structure. By opposition to the homogeneous coarse texture domain, this structure mimics an un-compacted soil composed of particles with a wide range of particles sizes. Hereon this structure will be referred to as HM (Homogeneous-Mix).

**Table 1** details the different arrangements of the four modeled structures, with information on their hydraulic properties and particles sizes. The sizes of the particles in the different modeled structures were determined upon real physical sizes of glass beads and coarse texture sand that were used in column experiments that will be presented in the next section. Saturation water content,  $\theta_s$ , was determined experimentally by measuring the volume of water needed to saturate the different media, which were packed in a known volume. In order to enable a complete drying of the media, by evaporation,  $\theta_r = 0$  was selected, as recently done by Zhou et al. (2021). Nevertheless, the model was tested for  $\theta_r$  values in the range of 0-0.07, and for all  $\theta_r$  values the simulated results were consistent, with small differences in cumulative evaporation (< 10%) and identical trends of water content and pressure head profiles. The van Genuchten parameter  $\alpha$  was determined according to Benson et al. (2014) that correlated  $\alpha$  to particles diameter. The van-Genuchten  $n$  parameter is affected by the degree of grain uniformity in the domain (Wang et al., 2017), where high  $n$  values indicate on high uniformity. Therefore,  $n$  was taken as 3 for the uniform layers, as it was the highest  $n$  value permitted by HYDRUS, while keeping the relative error in the water mass balance of the entire flow domain, at low values at the order of 1% and below. For the HM domain,  $n$  was arbitrarily chosen to be equal to 1.25 as the medium was composed of particles with various sizes. Hydraulic conductivity at saturation,  $K_s$  [cm/d], was determined by the Kozeny-Carman equation (Carman, 1937; Kozeny, 1927), as demonstrated by Weisbrod et al. (2013).

The hydraulic properties of a salt layer are unknown, excluding permeability,  $k$ , which was recently examined, and found to be at the order of  $4 \times 10^{-12} \text{ m}^2$ , for NaCl (Nachshon and Weisbrod, 2015; Piotrowski et al., 2020). The permeability was used to calculate the saturated hydraulic conductivity of the salt, by the relation between  $K_s$  and  $k$  (Kasenow, 2002):

$$K_s = \frac{k \cdot \rho \cdot g}{\mu} \quad (1)$$

where  $\mu$  [kg/ms] is the dynamic viscosity;  $\rho$  [kg/m<sup>3</sup>] is the liquid density; and  $g$  [m/s<sup>2</sup>] is gravity acceleration. For water,  $\rho = 1000 \text{ kg/m}^3$ , and  $\mu \sim 0.0009 \text{ kg/ms}$  (at 25°C).  $g = 9.8 \text{ m/s}^2$ , and for the NaCl permeability of  $4 \times 10^{-12} \text{ m}^2$   $K_s$  is equal to  $4.3 \times 10^{-5} \text{ m/s} = 376.0 \text{ cm/d}$ . Since no further information is available about the salt hydraulic properties, the van-Genuchten parameters of the salt layer were taken to be equal to loamy-sand soil, from the HYDRUS-1D library, due to the similar hydraulic conductivity that this soil (350.2 cm/d) has to the salt layer. Important to emphasize is that the model examined only the physical impact that a salt crust has on water flow process during S1 and did not account for the chemical aspects of high salinity and associated changes of the solution osmotic potential, surface tension and viscosity. Salt crust hydraulic properties are also depicted in **Table 1**.

The modeled domains had a depth of 10 cm and the upper boundary condition was set as atmospheric boundary, with potential evaporation of 0.65 cm/d (based on the data obtained in the laboratory glass-beads evaporation experiment, which will be detailed below). Lower boundary was set as zero flux and initial condition was set as full saturation throughout the entire column. Since HYDRUS solves the Richards equation, its results are valid only during S1 where evaporation occurs at the soil surface and there is a hydraulic continuity along the soil profile. Therefore, simulations were ceased once S1 was ended and the transition to S2 had begun.

375

**Table 1: Hydraulic parameters of the modeled setups.  $\theta_s$ ,  $\alpha$ ,  $K_s$ , and  $d$ , stand for water content at saturation ( $\text{cm}^3/\text{cm}^3$ ), the  $\alpha$  van-Genuchten parameter (1/cm), hydraulic conductivity at saturation (cm/d), and range of particles diameter (mm), respectively. Where not mentioned, the  $n$  van-Genuchten parameter is equal to 3 (-). For all simulations the tortuosity parameter in the conductivity function was taken to be equal to 0.5(-).**

Depth (mm)	SETUP			
	Homo-Coarse (HC)	Homo-Coarse-Compacted (HCC)	Homogeneous-Mix (HM)	Fine-Up (FU)
0-10	$\theta_s = 0.29$ $\alpha = 0.07$ $K_s = 5655$ $d = 0.4-0.5$	$\theta_s = 0.39$ $\alpha = 0.01$ $K_s = 233$ $d = 0.049 - 0.053$	$\theta_s = 0.28$ $\alpha = 0.05$ $n = 1.25$ $K_s = 3537$ $d = 0.09 - 1.3$	$\theta_s = 0.39$ $\alpha = 0.01$ $K_s = 233$ $d = 0.049 - 0.053$
10-20				$\theta_s = 0.36$ $\alpha = 0.02$ $K_s = 578$ $d = 0.090 - 0.106$
20-40		$\theta_s = 0.29$ $\alpha = 0.07$ $K_s = 5655$ $d = 0.4-0.5$		$\theta_s = 0.38$ $\alpha = 0.03$ $K_s = 2922$ $d = 0.18-0.212$
40-60		$\theta_s = 0.29$ $\alpha = 0.07$ $K_s = 5655$ $d = 0.4-0.5$		$\theta_s = 0.29$ $\alpha = 0.07$ $K_s = 5655$ $d = 0.4-0.5$
60-80		$\theta_s = 0.41$ $\alpha = 0.15$ $K_s = 14613$ $d = 1.0-1.3$		
80-100				
<b>Salt crust</b>				
2 mm above soil surface	$\theta_s = 0.41, \alpha = 0.124, n = 2.28, K_s = 350$			

380

The simulations were used to observe changes of the soil profile wetness and to compute length of S1 and the impact of compaction and salt precipitation on its length. The salt crust was simulated by adding a 2 mm layer of the crust on top of the modeled domains (this thickness is similar to the observed one corresponding to the depositing salt layers during



385 the experiments presented below). This layer was added after two days of evaporation, as it is experimentally known that the appearance of the salt crust is not instantaneous with the onset of evaporation.

Upper boundary condition of the simulated salt layer was as defined for the salt free setup, with atmospheric potential evaporation of 0.65 cm/day. Initial pressure head of -1000 cm  
390 was defined for the added salt layer, assuming it is dryer than the underlying soil. Model sensitivity to the initial pressure head of the salt crust was low, as it was tested for various levels in the range of -1000 to -100 cm and simulation results were identical, as after one time step the pressure head of the salt crust and resultant water content were adjusted in respect to the wetness of the underlying soil. Important to emphasize that the model of the  
395 FU structure was tested also for a more moderate change of the soil hydraulic properties, where the hydraulic properties of the five layers (**Table 1**) were interpolated, and evenly distributed, over 30 layers, 3 mm each. Results of the five layers and the 30 layers' structures were similar, hence hereon only the results of the five layers will be discussed, as they correspond to the experimental setup.

#### 400 **3.4. Impact of compaction on evaporation and salt precipitation**

Two sets of column-evaporation experiments were conducted: (i) columns filled with glass beads at varied arrangements, mimicking different conditions of non-compaction and compaction scenarios; and (ii) columns filled with coarse sand under compaction and non-compaction conditions. The glass beads experiments aimed to test the research hypothesis  
405 under synthetic and controlled conditions, whereas the coarse sand column experiments aimed to better correlate the synthetic structures results to a more natural setup, with a deeper soil profile.

The glass beads evaporation experiments were conducted on rectangular glass columns, 10 cm high, 5 cm width, and 2.5 cm aperture. Corresponding to the numerical models, the glass

410 beads experimental setups were identical to the HM and FU structures, as detailed in **Table 1**.  
In addition, in this set of experiments, a setup mimicking a tilled soil was examined also, and  
for this purpose, the tilled setup was constructed in a reverse order of the FU setup, with the  
largest glass beads being located at the top of the profile and the smallest beads at the  
bottom. Hereon this structure will be referred to as CU (Coarse-Up). The three different setups  
415 were saturated with distilled water (DI) or with a 10% (by weight) NaCl solution. All the  
evaporation experiments were carried out in two replicates. The packed columns were  
positioned on high resolution electronic scales ( $\pm 0.01$  gr, Adam; Shekel, Israel) in order to  
record mass changes, thus monitoring the cumulative water loss to evaporation. Small fans  
(Y.S. TECH, DC BRUSHLESS FAN, FD128020HB, DC12V, 0.15V) were installed  $\sim 3$  cm above the  
420 upper soil surfaces of the samples, pulling air upward. Along the process of evaporation,  
photos of the columns profiles were taken with a camera (UEye, Germany) at a rate of 6  
pictures per minute. Total duration of evaporation for each setup was about 12.5 days ( $\sim 303$   
hours). This set of columns experiments, and the corresponding numerical models detailed  
above, were carried out for columns shorter than the capillary lengths of the porous media  
425 under interest. Consequently, the resulting duration of S1 is affected by this physical constrain  
(Assouline et al., 2014). In order to extend and to validate the findings of the small columns  
experiments to more realistic conditions, the coarse sand columns experiments were  
conducted as detailed below.

The coarse sand experiments were conducted in circular columns, 92 cm long and 4.1 cm in  
430 diameter. The columns were filled with the same coarse sand used for the CT scans  
experiments. Soil compaction, which lowered the soil surface by 4 cm, was achieved as  
detailed in **section 3.2**. The columns were saturated from bottom, through a designated  
valve, by DI water or 10% NaCl solution. After saturation, the columns were placed in the  
laboratory under the small fans, as was done for the glass beads columns. Every few hours  
435 the columns were weighed on a 0.2 gr accuracy scale (Snowrex NHV-6, Sam hing scales

factory limited, Kowloon, Hong Kong). The experiment lasted for 250 hours, with two repetitions for the compacted and un-compacted DI setups. Even though not in the exactly similar dimensions, these setups correspond to the modeled HC and HCC structures.

#### 4. Results and Discussion

440 Experimental results are organized and presented first for the micro-scale, and then for the macro scale; considering the physical changes that the sand underwent due to compaction. Following that, the results representing the impact of compaction on the combined processes of evaporation and salt precipitation will be discussed.

##### 4.1. Micro-scale effects of compaction

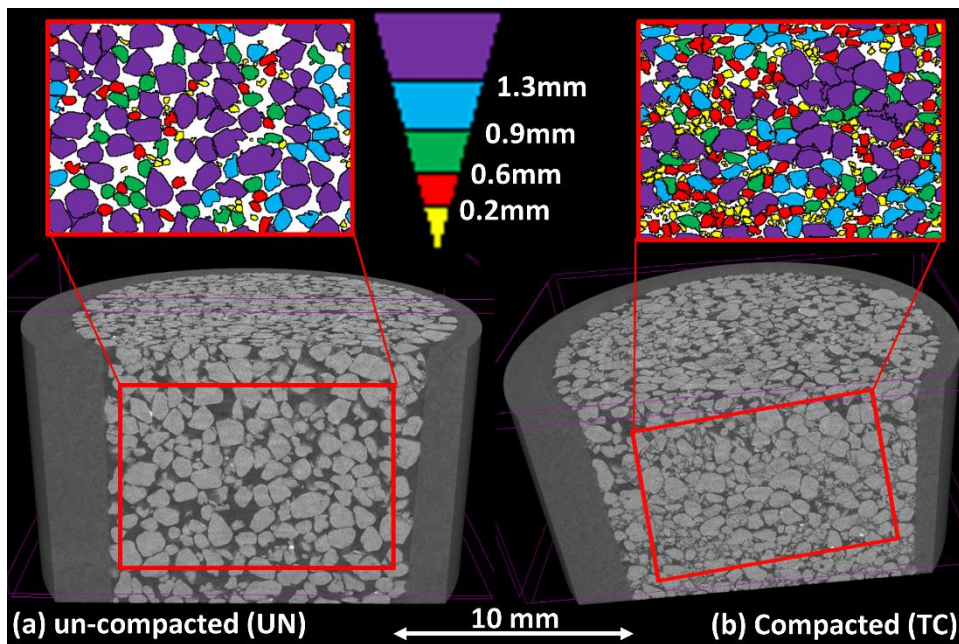
445 The impact of compaction on changes in grain and pore geometry, size and distribution, at the micro scale, were examined by producing 3D and 2D images (slices) of the sand domain using the  $\mu$ CT (**Figure 2**). The 2D slices were randomly selected along the vertical axis of the columns, and used to quantitatively analyze the different physical properties of pores and grains of the compacted and un-compacted samples. **Figure 3** presents the analysis process which was  
450 done for the 2D slices, in order to observe the changes in pore and sand grain properties following compaction at the top layer of the sample and at its bottom. **Figure 3a** shows representative images from: (i) a un-compacted sample (UN) at depth of 0-7 mm (**Figure 3a'**); (ii) the lower part of the compacted sample (LC; depth of 9-18 mm) (**Figure 3a''**); and (iii) the top part of the compacted sample (TC; depth of 0-7 mm) (**Figure 3a'''**). In the UN, as well as in  
455 the LC domain, the sand grains are relatively round and uniform in size. By comparison, in TC, there are areas with a high proportion of relatively small and more angular grains, a result of the grains breakage in specific locations (marked by the yellow contours in **Figure 3a'''**, and also depicted in **Figure 2**). Naturally, these changes in grain sizes also affect pore sizes and their spatial distribution, as visually observed in **Figure 2**, and depicted by the pores opening  
460 heat map (**Figure 3b**).

In **Figure 3c**, we demonstrate the changes in number of grains for a given area in the TC sample and the spatial distribution of these changes, in comparison to the UN and LC data. For this purpose, each 2D scan, of any state and depth, was divided into a matrix of rectangles, 1.06 mm by 0.73 mm each. In each rectangle, the number of sand grain centers was counted, and  
465 the rectangle was colored in accordance with the number of grain centers. In the presented images, the main colors for the LC and UN cases are blue and green, indicating about 3-4 grain centers per rectangle, with low variation in colors. However, for the TC case, there is a high variation in the color of the rectangles, with a relatively high number of yellow and red rectangles (>6 grain centers) adjacent to green-blue rectangles.

470 The five randomly selected images of 'UN', 'TC', and 'LC' states were averaged and analyzed, as demonstrated in **Figure 3**, to provide a corresponding quantitative analysis of the number of grains per unit area, grain size (2D area) and pore opening (distance between adjacent grains) (**Figure 4**). For simplicity, all of these values were normalized with respect to those corresponding to the UN state. In agreement with the visual observations, minor differences  
475 were measured with respect to the number of grains between the UN and LC states. However, a significant difference was measured with the TC samples, where the total number of grains per unit area was ~50% higher for TC compared to UN and LC (**Figure 4A**). Moreover, with respect to changes in grain sizes, there is no significant difference between UN and LC, but for the TC layer, the average size of the grains was ~35% lower compared to UN and LC cases. The  
480 same trend was measured also with respect to pore opening, as the pore average opening of the TC was lower by ~10% compared to the two other cases.

The analysis of the grain counting within the rectangles (**Figure 3c**) was also conducted for the five randomly selected images. Analysis of each image was used to generate a histogram describing how many rectangles contained the different numbers of grains (**Figure 4B**). For  
485 the UN and LC cases grain density was lower compared to the TC setup, where the former had

on average 2-2.5 grains per rectangle, whereas the latter had 4 grains per rectangle. Moreover, for the TC layers, in comparison with the LC and UN cases, the histogram shifts to the right, indicating a higher number of rectangles that contain 4 grains or more.



490

Figure 2: 3D visualization of the top ~10 mm of un-compacted (a) and compacted (b) sand samples. Red rectangles exemplify the cropping of the 2D slices off the 3D structure. The 2D colored slices present, visually, the different grain size distribution between the compacted and un-compacted samples. Grains sizes are in respect to the color-bar. In addition, it is seen in (b) that compaction reduced pores sizes, and increased grains angularity, due to breakage of the grains.

495

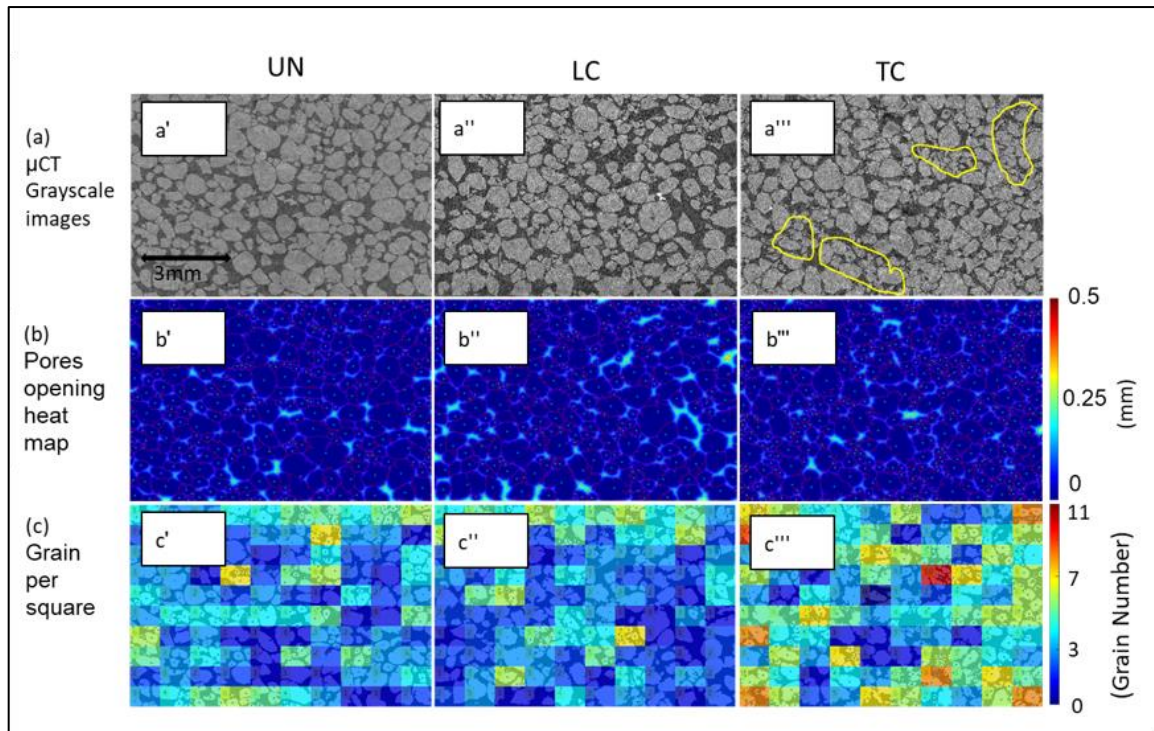
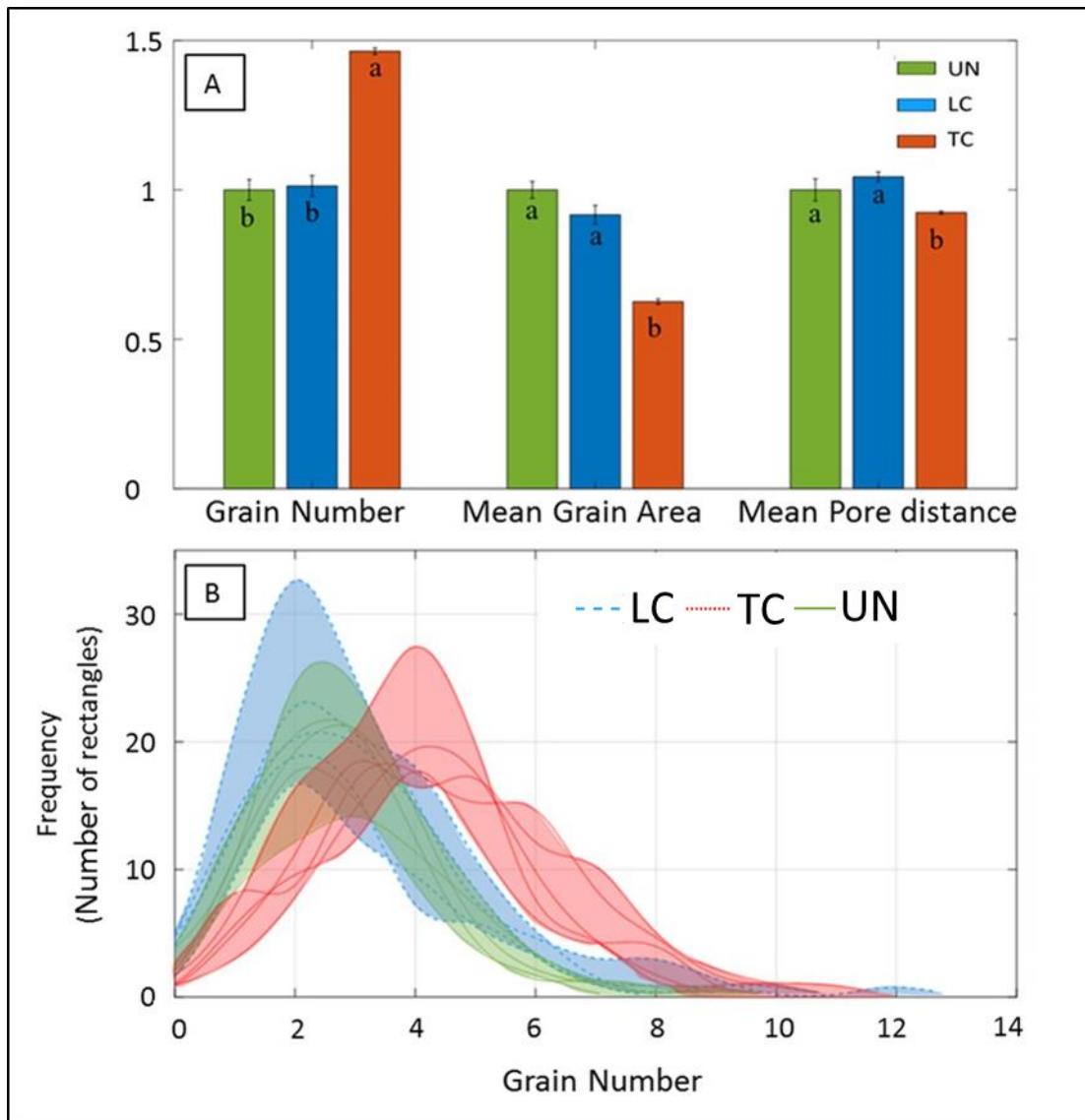


Figure 3: (a)  $\mu$ CT grayscale cross-sections scans; (b) pore opening heat maps; and (c) grain number spatial distribution maps, for the un-compacted ('), low ('') and top ('''') levels of compacted soil samples, respectively. Yellow contours in (a''') indicate areas with high levels of grain breakage. In (b), the blue dots represent the grain centers and the color bar indicates the distance within the pores from the nearest grain. In (c), the rectangles are colored in proportion to the number of grains in each one of them.

500



505

**Figure 4: (A) Average grain number, average grain area and average pore distance of the un-compacted soil sample (UN), low (LC) and top (TC) levels of compacted soil samples. Measured values were normalized in respect to UN. (B) Histogram represents grain number distribution of the un-compacted soil samples, and low and top levels of the compacted soil samples. In (B), each line is the histogram of a single slice and the colored areas represent the range of the five measured histograms, for each state.**

510

The presented image analyses, at the micro-scale, indicate the major impact that compaction has on the physical properties of the sand, close to the source of compaction (TC). It seems that compaction resulted in breakage due to friction of sand grains, leading to an increase in the grain number and their angularity, and a decrease in their mean size. In the deeper layer of the sand column (LC), the grains were practically not affected by the compaction and were similar to the control (UN) with respect to pore and grain sizes, shape and spatial distribution.

515

Moreover, it was shown that the compacted areas in the top layer were heterogeneously distributed (**Figure 3c, 4B**), in agreement with the concept of preferential propagation of the stress along the 'shear bands' (Naveed et al., 2016; Nawaz et al., 2013).  
520

#### 4.2. Macro-scale effects of compaction

At the macro scale, compaction effects were quantified by following the translocations of the colored sand grains, in the 10-cm-long transparent column. The translocation of the sand grains,  $\Delta L$  (mm), was calculated by measuring the distance of selected grains from the column's bottom at the initial state ( $L_0$ ) and following compression ( $L_C$ ), according to:  
525

$$\Delta L = L_C - L_0. \quad (2)$$

**Figure 5** presents  $\Delta L$  along the soil profile. Maximal translocation was observed within the upper layer of the soil profile, and it linearly decreases with depth, in agreement with the results reported by Schlüter and Vogel (2016). However, it is important to remember that translocation of the grains at each depth is the sum of all compaction processes that occurred below the point of interest, and that it does not necessarily indicate the degree of compaction (change of bulk density) at this point. In order to estimate the effect of compaction on the bulk density along the soil profile we estimated the changes in distance between adjacent grains,  $\Delta D$  (mm), in a similar way that was done for  $\Delta L$ :  
530

$$\Delta D = D_C - D_0 \quad (3)$$

where  $D_0$  and  $D_C$  are the measured distances between any adjacent selected grains, before and following compaction, respectively. Consequently, a negative  $\Delta D$  value indicates compaction and increase in bulk density, and vice versa.

Measurements of  $\Delta D$  indicate that compaction was not uniform along the sand profile (**Figure 5**), showing that certain depths were more severely compacted. At depths of 6, 17, 36, and 60 mm,  $\Delta D$  values were positive, indicating reduced bulk density at these specific locations.  
540



Maximal compaction of  $\Delta D = -1.3$  mm was measured at a depth of 32 mm, followed by  $\Delta D = -1.1$  mm at depth of 8 mm. Lower levels of the column were less compacted, excluding depths of 68 and 82 mm where  $\Delta D$  reached values of -1.0 and -0.8 mm, respectively.

545 This analysis further emphasizes the heterogeneous nature of soil compaction and the shear band effect, as different locations along the profile were more compacted compared to others. These differences are more notable at the macro scale, compared to the microscale observations, from the CT experiments. Nevertheless, it is evident that most of the profile underwent compaction, as most of the  $\Delta D$  values are negative, and that maximal compaction  
 550 was at the top  $\sim 30$  mm of the sample.

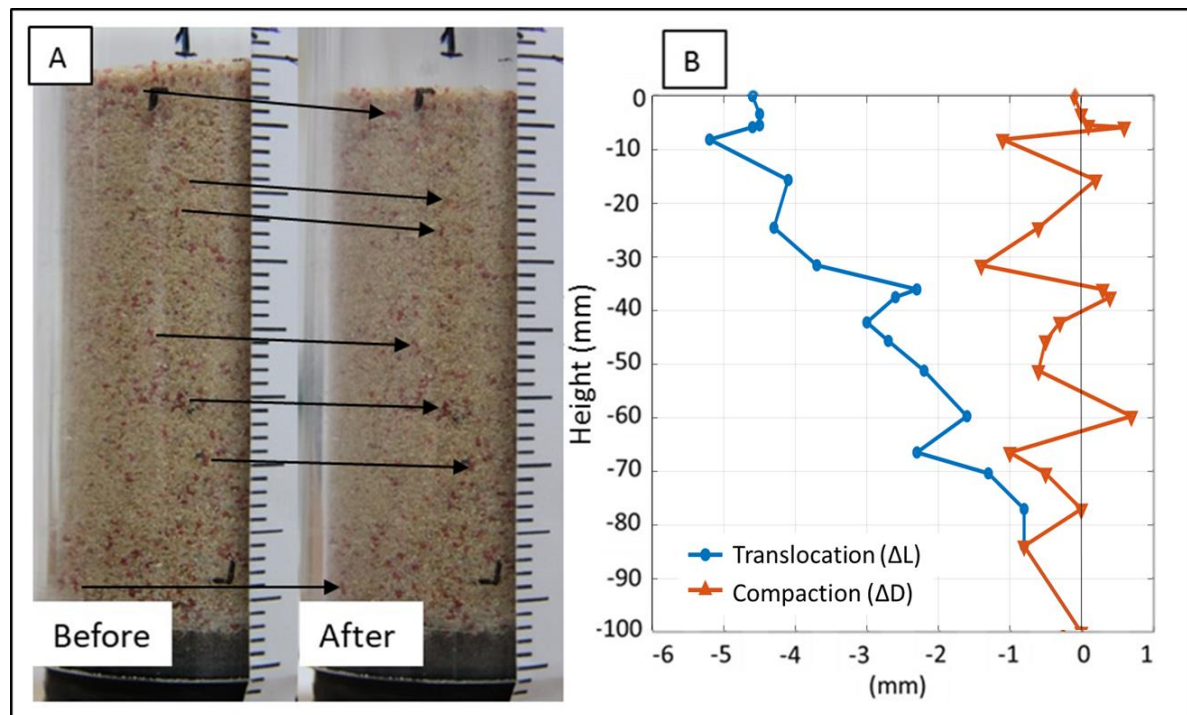


**Figure 5: (A) photos of the examined sand column 'Before' and 'After' compaction. Black arrows exemplify the vertical transition, due to compaction, of selected colored grains; (B) measured changes in grain translocation and compaction along the sand column.**

555 As seen from the micro and macro scales experiments, compaction induces the formation of a non-uniform soil profile, with smaller pores, smaller grains, and higher bulk density at the top levels of the soil profile, compared to the lower part of the profile. This structure is opposed to typical natural conditions, where the lower soil levels are those with the higher

bulk density (Campbell, 1994; Hernanz et al., 2000). Consequently, important hydrological  
560 processes such as infiltration and evaporation may be altered due to compaction. These  
aspects will be discussed in the following sections.

### 4.3. Numerical model

The HYDRUS-1D model results showed similar trends to those proposed in the conceptual  
model and in the research hypothesis, including the unique pattern of drying from bottom to  
565 top, for the simulated compacted structures, with the fine grains at the top (HCC, FU). **Figure  
6** presents the length of S1 for each one of the simulated structures, for conditions of with  
and without a salt crust. It is seen that for salt free conditions, the compacted structures had  
the longest S1 durations, with 136 hours for the FU structure, and 108 hours for the HCC setup.  
This was followed by the HC setup (96 hours), and the HM (72 hours). For all cases, the  
570 addition of the salt crust resulted in shortening of S1, yet the compacted structures had the  
longest S1 durations, also for the saline conditions, whereas, for the homogeneous structures,  
S1 durations were the shortest (**Figure 6**).

**Figure 7** displays water content distribution and effective hydraulic conductivity values along  
the modeled domains, 48 hours after evaporation onset. This time is also when the simulated  
575 salt crust was added, for the saline setups. These profiles give the physical explanation for the  
extended S1 duration of the compacted structures, for both with and without the addition of  
the salt crust. It is seen for the FU and HCC setups, that the fine grain texture domain on top  
of the coarse texture domain results in drying of the matrix from top to bottom, due to the  
stronger capillary suction of the finer pores. Consequently, higher water content levels are  
580 maintained close to the soil surface of the compacted setups, where evaporation is maximal,  
while the underlying coarse texture regions act a water reservoir to replenish evaporation  
(**Figure 7A**).

For all the considered cases, the addition of the salt crust resulted in reduction of S1, after some time, indicating on breaking of the hydraulic continuity between the underlying wet  
585 matrix and the salt crust. Also in this perspective, the elevated water content levels of the upper regions of the compacted structures resulted in higher levels of hydraulic conductivities (**Figure 7B**), which could support a capillary flow of liquid water from the deeper parts of the soil matrix to the salt crust and by that to maintain a longer S1, compared to the non-compacted setups.

590 Model results point on the high impact that the hydraulic properties of the simulated domain have on the evaporation dynamics. For example, notable differences were observed in between the two homogeneous and non-compacted setups, in respect to S1 length, wetness profiles, and impact of the salt crust on evaporation. These differences were a result of the different  $n$  values of the two domains, as most other hydraulic parameters were relatively  
595 similar. In addition, when the  $n$  value of the HM was elevated to be equal to the  $n$  value of HC - the simulated results were similar. Future studies should further explore these disparities and the sensitivities of the modeled systems to the different hydraulic parameters. However, for the purpose of this study, simulation results strengthen the conceptual model and research hypotheses (**Figure 1**), which were further explored by the following column  
600 experiments.

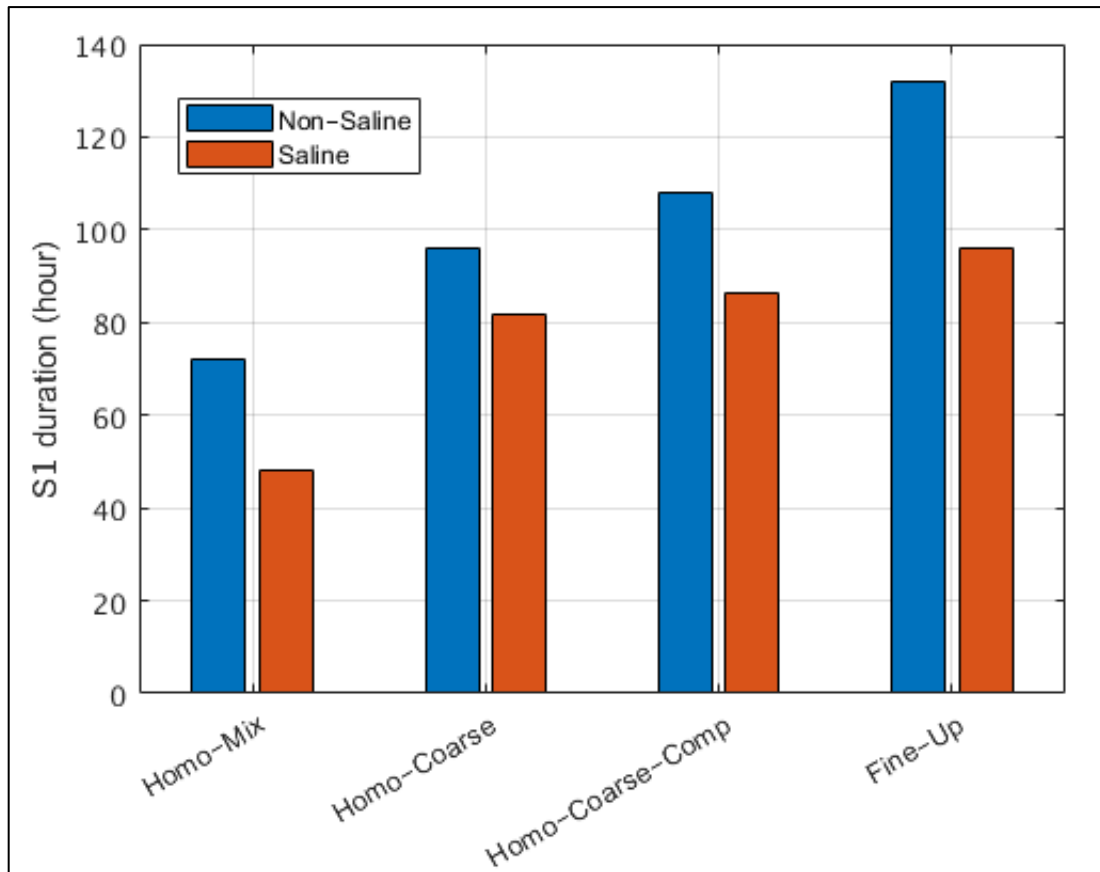
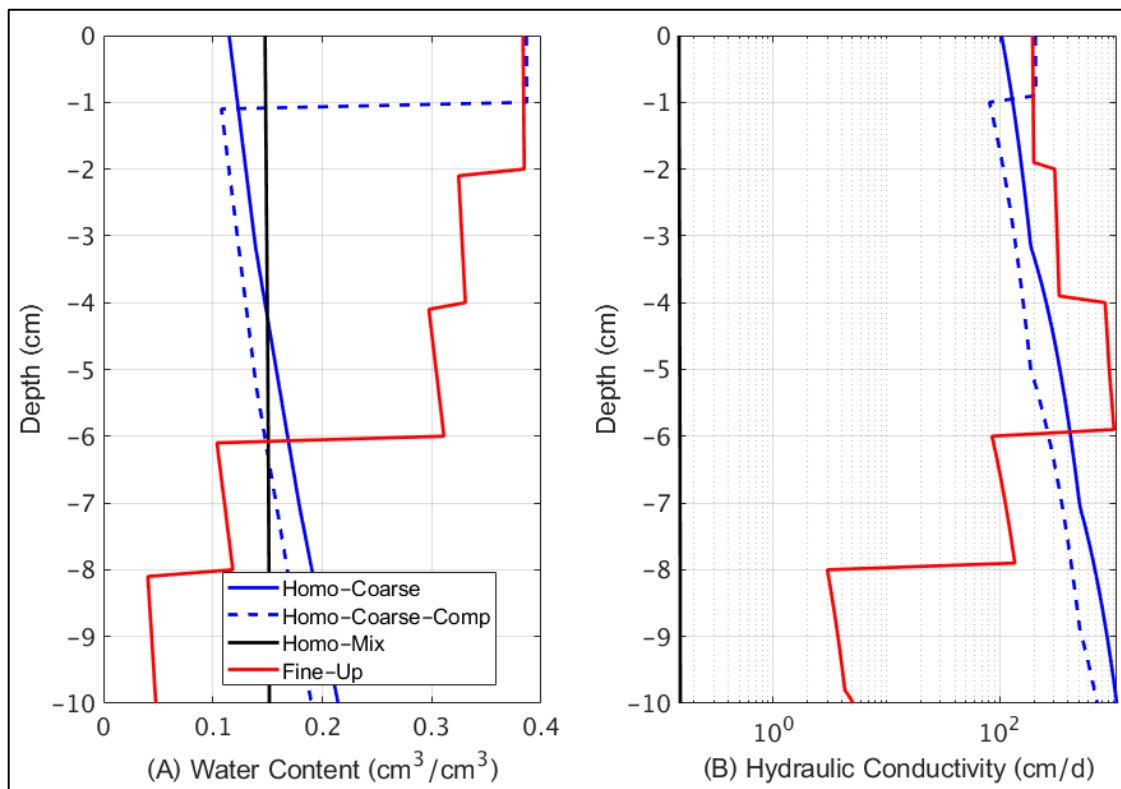


Figure 6: Duration of S1 for the four modeled setups, with and without the formation of the salt crust.



605 Figure 7: Simulation results of water content (A); and hydraulic conductivity (B) along the four modeled setups, 48 hours after evaporation onset.

#### 4.4. Evaporation and salt precipitation in layered glass beads domain

As aforementioned, glass beads were used to fill the rectangular columns as detailed in **Table 1**, to represent the compacted conditions (FU), and in a reverse order (CU) to mimic loose, e.g., tilled soil. The HM setup was also experimentally tested, representing a non-compacted structure with a wide range of particle size distribution. The evaporation process during the column experiments of the three glass beads configurations saturated with the saline solution is represented by a set of pictures in **Figure 8**. It is possible to follow the movement of the drying front for the homogeneous configuration (HM), and the compacted (FU) structure, which coincides with the numerical model results. Water flow and drying processes are also observed for the tilled (CU) setup.

For the HM structure, the evaporation front receded from top to bottom, as typically seen in evaporation of homogeneous porous media. A notable efflorescence salt crust is observed, in the image of 54 hours (**Figure 8A**), yet it is important to emphasize that salt precipitation started at about 15 hours following evaporation onset.

For the FU structure, the soil surface remained moist for the entire duration of the experiment, while the drying front progressed upward, from bottom to top (**Figure 8B**). The unique drying pattern of the FU structure, which mimics compacted soil, is a result of the hydraulic properties of the top layer that had the highest capillary suction along the soil profile. This structure results in a continuous upward flow of the solution from the coarser layers at the bottom that have a lower capillary suction. Replacement of water by air in the coarse texture layers points on air invasion into the matrix, from the soil surface, via air conduits which are likely to develop in the relatively larger pores of fine texture layer. A similar behavior was reported by Assouline and Narkis (2019) for DI water, where a detailed explanation of the impact of layered structure on evaporation is given. For the FU setup, under saline conditions, evaporation resulted in salt precipitation, at the soil surface, as observed in

here at the image taken after 54 hours of evaporation (**Figure 8B**). As detailed for the HM set, salt precipitation initiated after about 15 hours.

635 For the CU structure, air penetration into the coarse upper layer was observed after 14 hours of evaporation and a slow recession of the evaporation front downward was observed over time (**Figure 8C**). For the CU case, salt precipitation was minor, due to the receding evaporation front, with no formation of a salt crust on the surface, or inside the medium.

Measurements and recording of changes in column masses during the experiment enabled to compute average cumulative evaporation of the different setups, as presented in **Figure 9**.  
640 Maximal values of standard deviation, for each setup, are detailed in **Table 2**. Transition from S1 to S2, which is the time in which initial high and constant evaporation rate start to decrease, was marked on each cumulative evaporation curve in **Figure 9**. The transition times were determined by identifying the divergence of the curves from their tangents during initial stages of evaporation (see example for FU setup in **Figure 9**). The slope of each tangent line  
645 describes the initial (S1) evaporation rate of each curve.

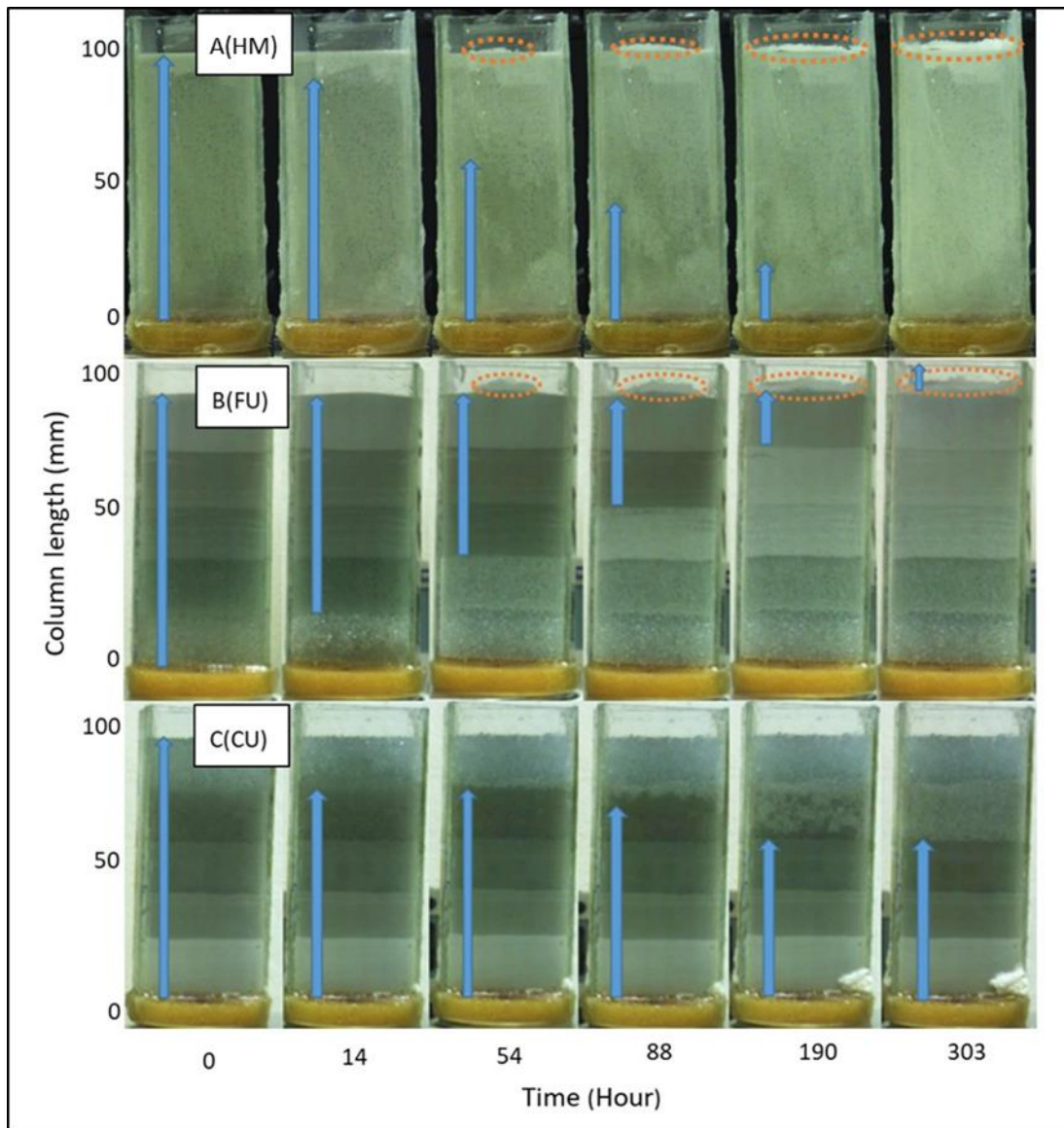
For the HM, the duration of S1 with DI water was about 46 hours, with a cumulative evaporation of ~14 mm. Total evaporation after 300 hours for the HM, DI water, was 23 mm. The relatively long S1 duration and high cumulative evaporation for HM, resulted in the formation of a notable efflorescence salt crust (**Figure 8a**), with a thickness of about 3.5 mm  
650 as estimated from the images. The saline conditions reduced the duration of S1 by more than 70%, and cumulative evaporation at the transition from S1 to S2 was lowered by more than 80%, compared to evaporation from initially DI saturated HM columns.

In agreement with the observed drying pattern (**Figure 8b**), it was shown that FU S1 was the longest compared to all other setups (**Figure 9**). S1 duration for the FU structure was of 66 and  
655 62 hours for the DI and saline conditions, respectively. Cumulative evaporation was also high for the FU setup, with 11 and ~18 mm at the end of S1, for the saline solution and DI

conditions, respectively, and total cumulative evaporation after 300 hours, of 26 mm for the saline solution, and 28 mm for the DI water. In comparison to the HM with DI water, the cumulative evaporation of the FU, after 300 hours, was 13% higher (**Figure 9**). The long  
660 duration of S1 for the FU, the persistence of the evaporation front at the surface of the column, and the corresponding high cumulative evaporation (**Figure 9**), led to the precipitation of a notable efflorescent salt crust (**Figure 8B**) with a thickness of about 6 mm as estimated from the images.

While saline conditions for the HM setup led to reduction of more than 50% in total  
665 evaporation and major changes in duration and cumulative evaporation of S1, for the FU setup, the impact of salinity was much less prominent. For the FU, the salinity reduced cumulative evaporation and the duration of S1 by less than 10%, and cumulative evaporation at the transition from S1 to S2 was reduced by less than 40% (**Figure 9**).

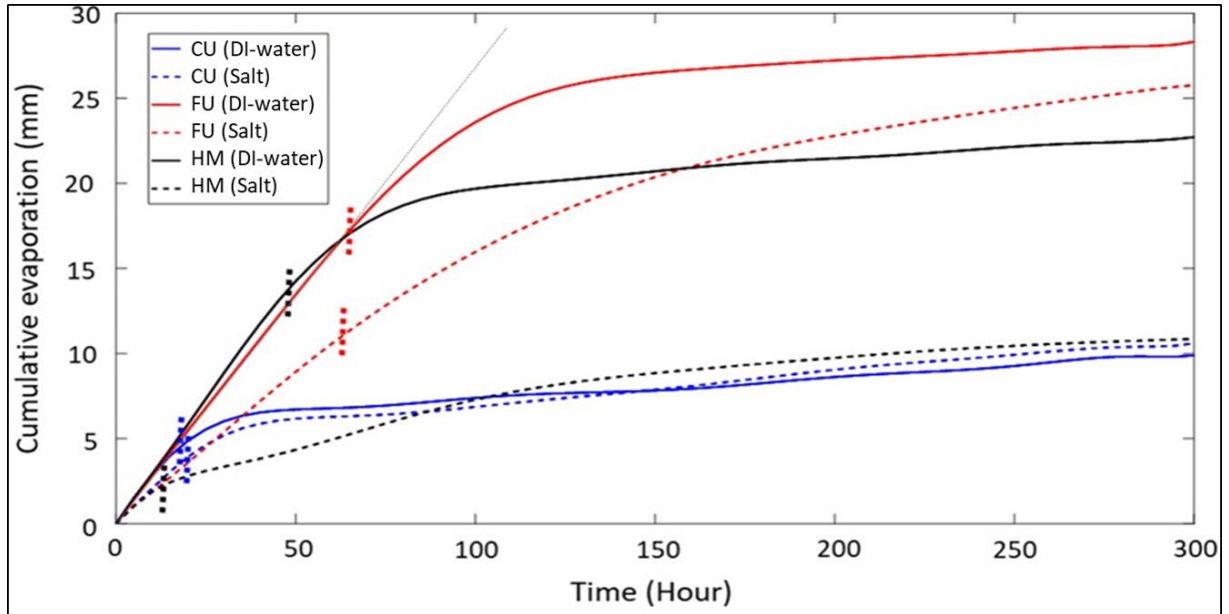
Unlike for the HM setup, the evaporation from the CU column showed a transition from S1 to  
670 S2 after ~19 hours of evaporation, and a cumulative evaporation of ~3.5 mm and ~4 mm (**Figure 9**), for the saline solution and DI water, respectively. These results and the relatively quick transition into S2, coincide with the receding of the drying front downward as seen in **Figure 8c**. During S2, evaporation was minimal, due to the low rate of vapor diffusion through the dry coarse porous medium at the surface, and total cumulative evaporation after 300  
675 hours was 10 mm, for both saline and DI conditions, which is less than half the cumulative evaporation of the HM setup and ~61% lower than the FU. As aforementioned, for the CU saline conditions, no salt crust was observed because of the receding evaporation front that did not support the processes of salinity buildup at the soil surface. The absence of the salt crust at the surface of the CU column explains the observed negligible difference in  
680 evaporation between the saline and DI water setups (**Figure 9**).



685 **Figure 8: Evaporation and salt precipitation patterns for: (A) HM – homogeneous mixture of the glass beads; (B) FU - with the fine glass beads at the upper levels; and (C) CU - with the coarse glass beads at the upper levels. Numbers at the bottom indicate time length of evaporation. Top and bottom of the blue arrows indicate the upper and lower boundaries of the saturated zones, respectively. The orange circle marks locations of salt precipitation.**

690





695 **Figure 9: Cumulative evaporation for the coarse up (CU), fine up (FU), and the homogeneous mixed (HM) structures, for conditions of DI water (solid lines) and saline solution (dashed lines). Vertical dotted lines indicate the transition from S1 to S2. Thin grey line is an example of a tangent line used to identify S1-S2 transition.**

**Table 2: Maximal values of standard deviation for cumulative evaporation measurements.**

	DI - Water [mm]	Saline solution [mm]
HM	5.833	3.312
FU	5.928	4.957
CU	1.297	0.676

700 **4.5. Differences in salinity impact on evaporation**

As shown above, the three different setups: HM, FU, and CU, responded differently for the saline conditions, with the greatest impact observed for the HM, followed by the FU, and the CU that presented minimal changes. **Figure 10** presents the relative change in cumulative evaporation for the different setups, over time. After ~5 hours of evaporation, all setups presented a reduction of about 30% in cumulative evaporation compared to the DI conditions. This reduction in evaporation may be a result of increased pore water NaCl concentration near the evaporation front at the surface of the columns, which results in reduction of the solution osmotic potential and vapor pressure. The 30% reduction coincides with the fact that vapor pressure of a saturated NaCl solution, at 25 °C is equal to 2.401 kPa, which is ~25% lower than the vapor pressure of pure water that is equal to 3.169 kPa (Lide, 2007). However, more

705

710

interestingly, after these first five hours, the relative impact of salinity on evaporation started to vary significantly, depending on the soil structural configurations.

The HM setup introduced a reduction in evaporation that was much greater than 25%, at the order of 60%, throughout most of the evaporation process, with a maximal reduction of ~70% after about 50 hours. Total reduction in cumulative evaporation at the end of the experiment was around 50% (**Figure 10**). For the FU setup, the reduction in cumulative evaporation was maintained at 30-35% for about 100 hours, which is approximately 35 hours longer than S1 duration of the DI setup (~65 hours). After ~100 hours, the difference between the saline and DI setups for FU was gradually moderated, along S2, and by the end of the experiment, total cumulative evaporation of the saline FU setup was only 10% lower compared to the DI state (**Figure 10**). For the CU setup, after the initial reduction of ~30% at the first five hours of evaporation, the difference between the saline and DI conditions decreased, to very low values, and after 150 hours of evaporation, no differences were observed (**Figure 10**).

For both HM and FU setups, the greatest difference in evaporation between the DI and saline conditions was observed during the time where the DI columns were at S1 and the saline solution configurations moved into S2. The large difference between the DI and saline condition for the HM during this time, at the order of 70%, indicates that the reduction of the solution vapor pressure is not the only mechanism that reduces evaporation. For the non-saline condition, the S1-S2 transition occurred after ~50 hours, for the HM setup. However, for the saline condition, S2 started after ~10 hours of evaporation only, with a minor cumulative evaporation at the order of 2mm.

From the HM-DI setup it is understood that at that time, the saline domain is moist enough to supply water to the upper atmosphere-domain interface and that S1 should be sustained. Therefore, it is concluded that the transition into S2 after ~10 hours, is likely a result of increased osmotic potential of the solution, salt precipitation and the development of the

efflorescent salt crust on top of the HM domain. The precipitated salt crust acts as a mulching layer that results in hydraulic discontinuity between the saturated domain and the atmosphere. Even though the matrix under the salt crust is moist enough to support S1 under salt free conditions, it is not wet enough to support liquid water flow into the salt crust, therefore vapor diffusion through the salt dictates the evaporation rate. This is in agreement with observations from previous studies (Gran et al., 2011; Nachshon and Weisbrod, 2015), and the numerical simulation.

For the FU setup, the fact that the differences in duration of S1 between the DI and saline conditions were minor (**Figure 9**), and the reduction in cumulative evaporation during S1 is at the order of 30-35%, suggests that the main mechanism that reduced evaporation was the reduction of the solution vapor pressure. The negligible impact of precipitated salt crust, for the FU setup, suggests that in this case the crust was hydraulically connected to the underlying media and that liquid water was flowing towards the surface of the salt crust, where the evaporation front was located. This hydraulic continuity suggests that the unique structure of the FU state, that mimics compacted soils, enables water from the lower layers of the drying profile to flow upward into and through the salt crust. It is suggested here that the hydraulic continuity between the precipitated salt crust and the underlying domain was possible for the FU and not for HM, due to the unique FU structure that keeps the upper layer of the domain wet, as also demonstrated by the numerical model (**Figure 7**).

For the CU setup, it is believed that during S1, the increase of the NaCl solution concentration at the evaporation front led to the observed reduction in evaporation at the order of 30%. This is in agreement with the vapor pressure reduction of a saturated NaCl solution. However, during S2 the differences between the DI and saline conditions decreased as vapor diffusivity, through the porous domain became the factor controlling evaporation, for both cases: with and without a salt crust.

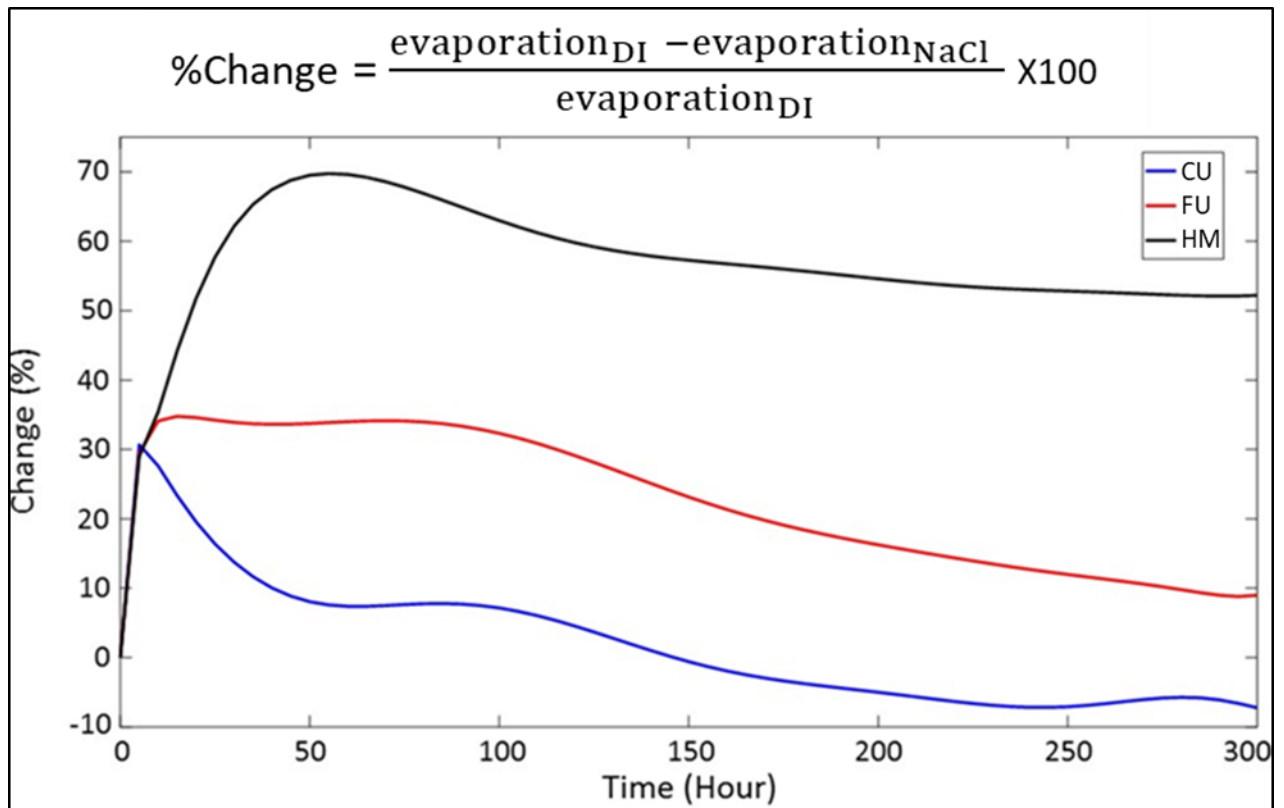


Figure 10: Relative difference in cumulative evaporation between saline and non-saline soil water solution over time, for the tilled (CU), homogeneous-mixed (HM), and compacted (FU) setups.

765

#### 4.6. Sand column experiments

The glass bead experiments and the numerical model supported the research hypothesis.

However, both consisted of a layered structure, assuming it is a reasonable approximation for compacted conditions. The advantage of using the layered structure (FU), with the fine texture

770

media overlying coarser texture domains, is the simplicity of constructing the domain under controlled, accurate, and reproducible conditions. However, in reality, soil compaction will form a more complex structure, as also shown here by the micro and macro scale compaction experiments. Moreover, while the HM setup represents a non-compacted homogeneous

775

domain with a wide range of particle size distribution, it fails to be an accurate non-compaction counterpart for the FU setup. As detailed in sections 4.1 and 4.2, compaction affects mainly the upper levels of the soil profile, while the deeper parts of the profile maintain their initial physical and hydrological properties. Therefore, the initial state of the FU setup, prior to compaction, should be composed of a homogeneous domain with a narrow range of

particle size distribution and with a texture similar to the lower levels of the FU profile.

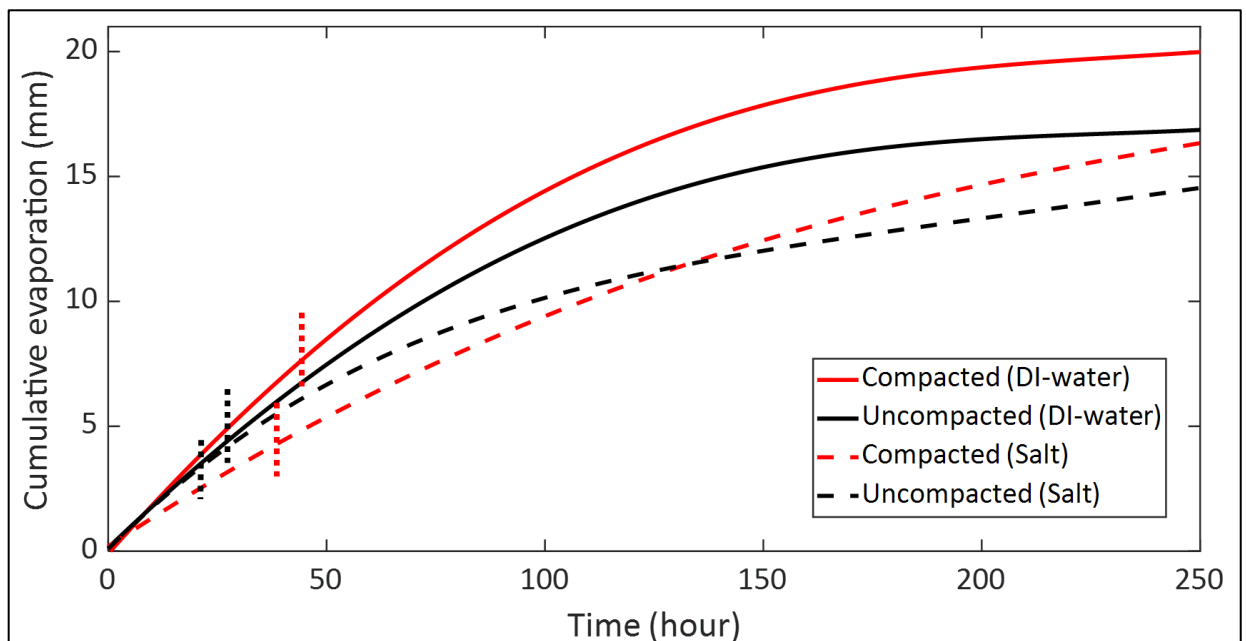
780 Therefore, in order to associate the findings of the glass bead experiments and simulations with real life conditions, and for more realistic length scales, the experiments considering compacted and un-compacted sand columns, with ~1m length, were conducted.

In agreement with the numerical model simulations and the glass bead experiments, it is seen that the compacted sand, with no salt, had the highest cumulative evaporation with total  
785 evaporation of  $20.0 \pm 0.23$  mm (**Figure 11**). For the un-compacted sand, maximal cumulative evaporation was equal to  $16.9 \pm 3.11$  mm. In respect to S1-S2 transition, in agreement with the layered structure results, it is seen that highest evaporation rate is measured for the DI compacted sand, with a notable reduction in evaporation rate observed after ~48 hours of evaporation, and cumulative evaporation of ~8 mm (**Figure 11**). For the un-compacted DI  
790 sand, transition into S2 with a notable reduction in evaporation rate was observed after ~25 hours of evaporation, with cumulative evaporation of about 4.5 mm (**Figure 11**).

For saline conditions, where salt precipitation was observed for both compacted and non-compacted setups, after S1, the compacted sand also displayed higher cumulative evaporation compared to the un-compacted state, with total cumulative evaporation of about  
795 16.5 mm and 14.5 mm, for the compacted and un-compacted samples, respectively (**Figure 11**). S1 duration of the compacted saline setup was approximately twice as long as the non-compacted saline domain (~40 hours vs 20 hours, respectively). However, cumulative evaporation during S1 was only ~40% higher for the compacted setup (~4.8 mm) compared to the non-compacted domain (~3.5 mm), indicating a lower evaporation rate during S1 for the  
800 saline-compacted setup, compared to all other setups. Future studies should clarify this disparity, yet it could be related to preferential water flows that may be developed in compacted soils (Zhang et al., 2018; Shein et al., 2003; Nagy et al., 2018), due to heterogeneous changes of the compacted soil texture and structure along the stress chains (Nawaz et al., 2013; Naveed et al., 2016). Consequently, evaporation may be concentrated in

805 specific locations at the soil surface and not homogeneously distributed as common for  
homogeneous domains. This may lead to elevated salt concentration in the pore water in the  
locations of concentrated evaporation, as demonstrated by Shokri-Kuehni et al. (2020). The  
resulting increased salt concentration increases the osmotic pressure and reduces vapor  
pressure of the solution, which reduces evaporation. It is likely that in the glass beads  
810 experiments this phenomenon was not observed since the glass beads layers were  
homogeneously packed.

Regardless the reduction of evaporation rate during S1 for the compacted saline setup, that  
should be further explored, this set of sand column experiments further strengthen the  
conceptual model and research hypothesis, as being presented in **Figure 1**, and indicates that  
815 the research findings are valid even though the soil profiles were relatively shallow.



820 **Figure 11: Cumulative evaporation for the compacted and un-compacted sand samples, for conditions of DI water (solid lines) and saline solution (dashed lines). Vertical dotted lines indicate the transition from S1 to S2.**

## 5. Summary and Conclusions

This study investigates the effect of compaction on sand physical properties at the micro and macro scales, and its impact on evaporation combined with salt precipitation processes.

Microscale properties such as the geometrical pore parameters were studied using X-ray  
825 computed micro-tomography ( $\mu$ CT) techniques by scanning sand samples before and after  
compaction. Compaction resulted in breakage of sand grains, reduced grain sizes, and pore  
average opening, mainly close to the source of compression. The spatial distribution of grain  
number, for the top levels of the compacted domain, has a higher proportion of areas with  
more grain numbers than the non-compacted and the lower levels of the compacted samples.  
830 These results illustrate the non-uniform spatial distribution of the physical changes that the  
soil undergoes through compaction. The impact of compaction decreases with depth, away  
from the source of compression.

Macro-scale soil compaction changes were evaluated by analyzing images that captured the  
movement of colored sand grains, and measuring their translocation before and after  
835 compaction. The highest translocation was at the upper levels of the soil profile, and with  
depth, translocation decreased. The distances between adjacent selected grains, before and  
following compaction, indicated that compaction is not uniform along the sand profile, with  
certain levels compacted more than others, strengthening the assumption of the  
heterogeneous nature of soil compaction and the shear band effect.

840 Since compaction affects the particle arrangement along the profile in a non-uniform manner,  
with maximal compaction at the relatively high layers of the soil profile, the impact of  
compaction on combined evaporation and salt precipitation was observed over two setups  
that were considered as compacted domains: (i) layered columns packed with glass beads with  
increasing size with depth (FU); and (ii) a coarse texture sand samples which were manually  
845 compressed from the top. In compression, three setups were considered as non-compacted  
domains: (i) a homogeneous column packed with mixed glass beads, with a wide range of  
particles size distribution (HM); (ii) a layered glass beads column where the glass beads sizes  
decreased with depth, representing a tilled soil profile (CU); and (iii) a homogenous coarse

sand sample. The cumulative evaporation measurements and the visual observations pointed  
850 to the significant impact of the different configurations on combined processes of evaporation  
and salt precipitation.

Glass beads experiments and numerical simulations have shown that for the HM structure,  
the drying front recedes from top to bottom, as expected for evaporating homogeneous  
porous media. The relatively long S1 duration and high cumulative evaporation of the HM  
855 setup resulted in a notable precipitation of an efflorescence salt crust at its upper surface. The  
precipitated salt layer resulted in a sharp decrease in evaporation rate since hydraulic  
continuity to the surface is lost, and the slow process of vapor diffusion through the salt layer  
controls evaporation.

For the FU, the drying front propagated from bottom to top, as demonstrated both  
860 experimentally and by the numerical simulation. S1 duration of the FU was long for the saline  
and DI water, and the cumulative evaporation was high. In the glass beads experiment, a  
prominent efflorescent salt crust was precipitated at the FU upper surface, due to the long S1  
and resultant high cumulative evaporation. However, in contrast to the HM, even though a  
notable salt layer was observed, its impact on evaporation at the FU structure was moderated  
865 compared to its impact for the HM setup. This is attributed to the stronger capillary suction of  
the upper layers, at the FU structure, which pumps water from the underlying levels upwards,  
maintaining high saturation at the soil surface, which supports liquid water continuity from  
the soil to the evaporation front, at the salt crust upper surface.

For CU setup experiment, a moderate recession of the evaporation front downward occurred  
870 over time like in the HM configuration, and loss of hydraulic continuity to the surface was  
achieved relatively early. Thus, the cumulative evaporation was low, salt precipitation was  
minor and therefore negligible differences in evaporation between saline and non-saline  
conditions were observed.



Results of the sand columns experiments were in good agreement with the glass beads  
875 columns experiments and the numerical simulations. This concurrence between the different  
experiments and the simulations further supporting the model and research hypothesis, as  
being presented in **Figure 1**, and support the assumption that the layered FU structure was a  
good approximation of compacted soil conditions. Nevertheless, it is important to emphasize  
that in real field conditions soil textures, environmental conditions, and compaction processes  
880 are much more complicated than those examined in this work. Therefore – further studies  
under more realistic conditions are needed.

This work sheds new light on the impact that soil compaction, which is a common feature in  
arable lands, has on bare soil evaporation processes, for saline and non-saline conditions. The  
885 insights gained from this study indicate that one may consider the use of different agricultural  
practices to control the degree of soil compaction, to the benefit of the water regime in the  
root zone.

## 6. References

Akker, J.J.H., Canarache, A.: Two European concerted actions on subsoil compaction.  
890 Landnutzung und Landentwicklung 42, 15–22,2001.

Alaoui, A., Lipiec, J. and Gerke, H. H.: A review of the changes in the soil pore system due to  
soil deformation: A hydrodynamic perspective, Soil Tillage Res., 115–116, 1–15,  
doi:10.1016/j.still.2011.06.002, 2011.

895

Alaoui, A., Rogger, M., Peth, S. and Blöschl, G.: Does soil compaction increase floods? A review,  
J. Hydrol., 557(January), 631–642, doi:10.1016/j.jhydrol.2017.12.052, 2018.

de Almeida, W. S., Panachuki, E., de Oliveira, P. T. S., da Silva Menezes, R., Sobrinho, T. A. and  
900 de Carvalho, D. F.: Effect of soil tillage and vegetal cover on soil water infiltration, *Soil Tillage  
Res.*, 175(June 2017), 130–138, doi:10.1016/j.still.2017.07.009, 2018.

Assouline, S.: Rainfall-Induced Soil Surface Sealing: A Critical Review of Observations,  
Conceptual Models, and Solutions, *Vadose Zo. J.*, 3(2), 570–591, doi:10.2136/vzj2004.0570,  
905 2004.

Assouline, S.: Modeling the Relationship between Soil Bulk Density and the Hydraulic  
Conductivity Function, *Vadose Zo. J.*, 5(2), 697–705, doi:10.2136/vzj2005.0084, 2006a.

910 Assouline, S.: Modeling the Relationship between Soil Bulk Density and the Water Retention  
Curve, *Vadose Zo. J.*, 5(2), 554–563, doi:10.2136/vzj2005.0083, 2006b.

Assouline, S. and Kamai, T.: Liquid and Vapor Water in Vadose Zone Profiles Above Deep  
Aquifers in Hyper-Arid Environments, *Water Resour. Res.*, 55(5), 3619–3631,  
915 doi:10.1029/2018WR024435, 2019.

Assouline, S. and Narkis, K.: Evaporation From Multilayered Heterogeneous Bare Soil Profiles,  
*Water Resour. Res.*, 55(7), 5770–5783, doi:10.1029/2018wr024560, 2019.

920 Assouline, S. and Or, D.: Anisotropy factor of saturated and unsaturated soils, *Water Resour.  
Res.*, 42(12), 1–11, doi:10.1029/2006WR005001, 2006.

Assouline, S., Selker, J. S. and Parlange, J. Y.: A simple accurate method to predict time of  
ponding under variable intensity rainfall, *Water Resour. Res.*, 43(3), 1–10,

925 doi:10.1029/2006WR005138, 2007.

Assouline, S., Narkis, K., Gherabli, R., Lefort, P. and Prat, M.: Analysis of the impact of surface layer properties on evaporation from porous systems using column experiments and modified definition of characteristic length, , doi:10.1111/j.1752-1688.1969.tb04897.x, 2014.

930

Augeard, B., Assouline, S., Fonty, A., Kao, C. and Vauclin, M.: Estimating hydraulic properties of rainfall-induced soil surface seals from infiltration experiments and X-ray bulk density measurements, *J. Hydrol.*, 341(1–2), 12–26, doi:10.1016/j.jhydrol.2007.04.018, 2007.

935 Barik, K., Aksakal, E. L., Islam, K. R., Sari, S. and Angin, I.: Spatial variability in soil compaction properties associated with field traffic operations, *Catena*, 120, 122–133, doi:10.1016/j.catena.2014.04.013, 2014.

Benson, C. H., Chiang, I., Chalermyanont, T. and Sawangsuriya, A.: Estimating van Genuchten  
940 Parameters  $\alpha$  and  $n$  for Clean Sands from Particle Size Distribution Data. From Soil Behavior Fundamentals to Innovations in Geotechnical Engineering., doi:10.1061/9780784413265.033, 2014.

Berezniak, A., Ben-Gal, A., Mishael, Y. and Nachshon, U.: Manipulation of Soil Texture to  
945 Remove Salts from a Drip-Irrigated Root Zone, *Vadose Zo. J.*, 17(1), 170019, doi:10.2136/vzj2017.01.0019, 2018.

Bergstad, M., Or, D., Withers, P. J. and Shokri, N.: The influence of NaCl concentration on salt precipitation in heterogeneous porous media, *Water Resour. Res.*, 53, 1702–1713,  
950 doi:10.1002/2016WR020060, 2017.

Bergstad, M., Or, D., Withers, P. J. and Shokri, N.: Evaporation Dynamics and NaCl Precipitation on Capillarity-Coupled Heterogeneous Porous Surfaces, *Water Resour. Res.*, 54(6), 3876–3885, doi:10.1029/2018WR022614, 2018.

955

Bresson, L. M., Moran, C. J. and Assouline, S.: Use of Bulk Density Profiles from X-Radiography to Examine Structural Crust Models, *Soil Sci. Soc. Am. J.*, 68(4), 1169–1176, doi:10.2136/sssaj2004.1169, 2004.

960 Brutsaert, W.: *Hydrology: An Introduction*, Cambridge Univ. Press, New York., 2005.

Campbell, D. J.: Determination and Use of Soil Bulk Density in Relation to Soil Compaction, *Dev. Agric. Eng.*, 11(C), 113–139, doi:10.1016/B978-0-444-88286-8.50014-3, 1994.

965 Carman, P. C.: Fluid flow through a granular bed. *Transactions of the Institution of Chemical Engineers*, , 15, 150–156, 1937.

Collins, T. J.: ImageJ for microscopy. *BioTechniques*, 43(1): 25–27,2007.

970 Dejong-Hughes, J., Moncrief, J., Voorhees, W. . and Swan, J. .: soil compaction causes effects and control, 1–16, 2001.

Gran, M., Carrera, J., Olivella, S. and Saaltink, M. W.: Modeling evaporation processes in a saline soil from saturation to oven dry conditions, *Hydrol. Earth Syst. Sci.*, 15(7), 2077–2089,

975 doi:10.5194/hess-15-2077-2011, 2011.

Hamza, M. A. and Anderson, W. K.: Soil compaction in cropping systems: A review of the nature, causes and possible solutions, *Soil Tillage Res.*, 82(2), 121–145, doi:10.1016/j.still.2004.08.009, 2005.

980

Hendrickx, J. M. and Flury, M.: Uniform and preferential flow mechanisms in the vadose zone., *Concept. Model. Flow Transp. Fract. Vadose Zo. Natl. Acad. Press. Washington, D.C*, 149–187, 2001.

985 Hernanz, J. L., Peixoto, H., Cerisola, C. and Sánchez-Girón, V.: An empirical model to predict soil bulk density profiles in field conditions using penetration resistance, moisture content and soil depth, *J. Terramechanics*, 37(4), 167–184, doi:10.1016/S0022-4898(99)00020-8, 2000.

Hillel, D.: *Introduction to Soil Physics.*, Academic Press, London., 1980.

990

Hopmans, J. W., Qureshi, A. S., Kisekka, I., Munns, R., Grattan, S. R., Rengasamy, P., Ben-Gal, A., Assouline, S., Javaux, M., Minhas, P. S., Raats, P. A. C., Skaggs, T. H., Wang, G., De Jong van Lier, Q., Jiao, H., Lavado, R. S., Lazarovitch, N., Li, B. and Taleisnik, E.: *Critical knowledge gaps and research priorities in global soil salinity.*, 2021.

995

Horn, R., Domial, H., Slowihka-Jurkiewicz, A. and Van Ouwerkerk, C.: *Soil compaction processes and their effects on the structure of arable soils and the environment*, Elsevier Sci. B.V. *Soil Tillage Res.*, 35(35), 23–36, doi:10.1016/0167-1987(95)00479-C, 1995.

1000 Horton, R., Ankeny, M. . and Allmaras, R. .: *Effects of Compaction on Soil Hydraulic Properties*, in *Soil Compaction in Crop Production*, pp. 141–165., 1994.

Kamai, T. and Assouline, S.: Evaporation From Deep Aquifers in Arid Regions: Analytical Model for Combined Liquid and Vapor Water Fluxes, *Water Resour. Res.*, 54(7), 4805–4822, doi:10.1029/2018WR023030, 2018.

1005

Kampf, S. K., S. W. Tyler, C. A. Ortiz, J. F. Muñoz, and P. L. Adkins.: Evaporation and land surface energy budget at the Salar de Atacama, Northern Chile. *Journal of Hydrology*. 310(1-4): 236-252,2005.

1010

Kasenow, M.: Determination of hydraulic conductivity from grain size analysis., *Water Resources Publication*, New York., 2002.

Keller, T., Lamandé, M., Peth, S., Berli, M., Delenne, J. Y., Baumgarten, W., Rabbel, W., Radjai, F., Rajchenbach, J., Selvadurai, A. P. S. and Or, D.: An interdisciplinary approach towards improved understanding of soil deformation during compaction, *Soil Tillage Res.*, 128, 61–80, doi:10.1016/j.still.2012.10.004, 2013.

1015

Keller, T., Sandin, M., Colombi, T., Horn, R. and Or, D.: Historical increase in agricultural machinery weights enhanced soil stress levels and adversely affected soil functioning, *Soil Tillage Res.*, 194(June), doi:10.1016/j.still.2019.104293, 2019.

1020

Kozeny, J.: Uber kapillare Leitung des Wassers im Boden. *Sitzungsber. Akad. Wiss.*, 136, 271–306, 1927.

1025

Lehmann, P. and Or, D.: Evaporation and capillary coupling across vertical textural contrasts in porous media, *Phys. Rev. E - Stat. Nonlinear, Soft Matter Phys.*, 80(4), 1–13, doi:10.1103/PhysRevE.80.046318, 2009.

1030 Lehmann, P., Assouline, S. and Or, D.: Characteristic lengths affecting evaporative drying of porous media, *Phys. Rev. E - Stat. Nonlinear, Soft Matter Phys.*, 77(5), 1–16, doi:10.1103/PhysRevE.77.056309, 2008.

Lide, R. D. (ed. ): *CRC Handbook of Chemistry and Physics.*, CRC, Boca Raton., 2007.

1035

Lipiec, J. and St e pniewski, W.: Effects of soil compaction and tillage systems on uptake and losses of nutrients, *Soil Tillage Res.*, 35(1–2), 37–52, doi:10.1016/0167-1987(95)00474-7, 1995.

1040 Mossadeghi-Björklund, M., Arvidsson, J., Keller, T., Koestel, J., Lamandé, M., Larsbo, M. and Jarvis, N.: Effects of subsoil compaction on hydraulic properties and preferential flow in a Swedish clay soil, *Soil Tillage Res.*, 156, 91–98, doi:10.1016/j.still.2015.09.013, 2016.

Mossadeghi-Björklund, M., Jarvis, N., Larsbo, M., Forkman, J. and Keller, T.: Effects of  
1045 compaction on soil hydraulic properties, penetration resistance and water flow patterns at the soil profile scale, edited by M. Goss, *Soil Use Manag.*, 35(3), 367–377, doi:10.1111/sum.12481, 2018.

Nachshon, U.: Seepage weathering impacts on erosivity of arid stream banks: A new  
1050 conceptual model, *Geomorphology*, 261, 212–221, doi:10.1016/j.geomorph.2016.03.011, 2016.

Nachshon, U.: Cropland soil salinization and associated hydrology: Trends, processes and examples, *Water (Switzerland)*, 10(8), doi:10.3390/w10081030, 2018.

1055

Nachshon, U. and Weisbrod, N.: Beyond the Salt Crust: On Combined Evaporation and Subflorescent Salt Precipitation in Porous Media, *Transp. Porous Media*, 110(2), 295–310, doi:10.1007/s11242-015-0514-9, 2015.

1060 Nachshon, U., Weisbrod, N., Dragila, M. I. and Grader, A.: Combined evaporation and salt precipitation in homogeneous and heterogeneous porous media, *Water Resour. Res.*, 47(3), 1–16, doi:10.1029/2010WR009677, 2011a.

Nachshon, U., Shahraeeni, E., Or, D., Dragila, M. and Weisbrod, N.: Infrared thermography of  
1065 evaporative fluxes and dynamics of salt deposition on heterogeneous porous surfaces, *Water Resour. Res.*, 47(12), 1–16, doi:10.1029/2011WR010776, 2011b.

Nagy, V., Šurda, P., Lichner, Ľ., Kovács, A. J., and Milics, G.: Impact of soil compaction on water content in sandy loam soil under sunflower. *J. Hydrol. Hydromech.* 66(4): 416-420, 2018.

1070

Nassar, I. N. and Horton, R.: Heat, Water, and Solute Transfer in Unsaturated Porous Media: I - Theory Development and Transport Coefficient Evaluation, *Transp. Porous Media*, 27(1), 17–38, doi:10.1023/A:1006583918576, 1997.

1075 Nassar, I. N. and Horton, R.: Salinity and compaction effects on soil water evaporation and water and solute distributions, *Soil Sci. Soc. Am. J.*, 63(4), 752–758, doi:10.2136/sssaj1999.634752x, 1999.

Naveed, M., Schjønning, P., Keller, T., de Jonge, L. W., Moldrup, P. and Lamandé, M.:  
1080 Quantifying vertical stress transmission and compaction-induced soil structure using sensor



mat and X-ray computed tomography, *Soil Tillage Res.*, 158(October 2017), 110–122, doi:10.1016/j.still.2015.12.006, 2016.

1085 Nawaz, M. F., Bourrié, G. and Trolard, F.: Soil compaction impact and modelling. A review, *Agron. Sustain. Dev.*, 33(2), 291–309, doi:10.1007/s13593-011-0071-8, 2013.

Nield, J. M., R. G. Bryant, G. F. Wiggs, J. King, D. S. Thomas, F. D. Eckardt, and R. Washington.: The dynamism of salt crust patterns on playas. *Geology*. 43(1): 31-34, 2015.

1090 Or, D., Lehmann, P., Shahraeeni, E. and Shokri, N.: Advances in Soil Evaporation Physics-A Review, *Vadose Zo. J.*, 12(4), vzj2012.0163, doi:10.2136/vzj2012.0163, 2013.

1095 Or, D., P. Lehmann., and N. Shokri, N.: Characteristic lengths affecting evaporation from heterogeneous porous media with sharp textural boundaries. *Estudios de la Zona No Saturada del Suelo*, 8, 1-8, 2007.

Otsu, N.: A Threshold Selection Method from Gray-Level Histograms, *IEEE Trans. Syst. Man. Cybern.*, 9(1), 62–66, doi:10.1109/TSMC.1979.4310076, 1979.

1100 Pagliai, M., Marsili, A., Servadio, P., Vignozzi, N. and Pellegrini, S.: Changes in some physical properties of a clay soil in Central Italy following the passage of rubber tracked and wheeled tractors of medium power, *Soil Tillage Res.*, 73(1–2), 119–129, doi:10.1016/S0167-1987(03)00105-3, 2003.

1105 Piotrowski, J., Huisman, J. A., Nachshon, U., Pohlmeier, A. and Vereecken, H.: Gas permeability of salt crusts formed by evaporation from Porous media, *Geosci.*, 10(11), 1–19,

doi:10.3390/geosciences10110423, 2020.

1110 Podder, M., M. Akter, A. S. M. Saifullah, and S. Roy.: Impacts of plough pan on physical and  
chemical properties of soil. *Journal of Environmental Science and Natural Resources*. 5(1),  
289-294, 2012.

Prat, M.: Recent advances in pore-scale models for drying of porous media, *Chem. Eng. J.*,  
86(1–2), 153–164, doi:10.1016/S1385-8947(01)00283-2, 2002.

1115

Rad, M. N. and Shokri, N.: Nonlinear effects of salt concentrations on evaporation from porous  
media, , 39(January), 1–5, doi:10.1029/2011GL050763, 2012.

Rasmussen, K. J.: Impact of ploughless soil tillage on yield and soil quality: A Scandinavian  
1120 review, *Soil Tillage Res.*, 53(1), 3–14, doi:10.1016/S0167-1987(99)00072-0, 1999.

Reicosky, D. C., Voorhees, W. B. and Radke, J. K.: Unsaturated Water Flow Through a Simulated  
Wheel Track<sup>1</sup>, *Soil Sci. Soc. Am. J.*, 45(1), 3, doi:10.2136/sssaj1981.03615995004500010001x,  
1981.

1125

Schlüter, S. and Vogel, H. J.: Analysis of soil structure turnover with garnet particles and X-Ray  
microtomography, *PLoS One*, 11(7), 1–17, doi:10.1371/journal.pone.0159948, 2016.

Shah, A. N., Tanveer, M., Shahzad, B., Yang, G., Fahad, S., Ali, S., Bukhari, M. A., Tung, S. A.,  
1130 Hafeez, A. and Souliyanonh, B.: Soil compaction effects on soil health and crop productivity:  
an overview, *Environ. Sci. Pollut. Res.*, 24(11), 10056–10067, doi:10.1007/s11356-017-8421-  
y, 2017.

Shein, E. V., Umarova, A. B., Dembovetskii, A. V., and Samoilo, A. A.: Effect of subsoil  
1135 compaction on the hydraulic processes in landscapes. *International agrophysics*. 17(3): 117-  
122, 2003.

Shokri-kuehni, S. M. S., Norouzi, M., Webb, C., Shokri, N., Zeiss, C. and Llc, M.: Impact of type  
of salt and ambient conditions on saline water evaporation from porous media. *Advances in*  
1140 *Water Resources* Impact of type of salt and ambient conditions on saline water evaporation  
from porous media, 105, 154–161, doi:10.1016/j.advwatres.2017.05.004, 2017.

Shokri-Kuehni, S. M. S., Vetter, T., Webb, C. and Shokri, N.: New insights into saline water  
evaporation from porous media: Complex interaction between evaporation rates,  
1145 precipitation, and surface temperature, *Geophys. Res. Lett.*, 44(11), 5504–5510,  
doi:10.1002/2017GL073337, 2017.

Shokri-Kuehni, S. M., Raaijmakers, B., Kurz, T., Or, D., Helmig, R., and Shokri, N.: Water table  
depth and soil salinization: From pore-scale processes to field-scale responses. *Water*  
1150 *resources research*. 56(2): e2019WR026707, 2020.

Shokri, N., Lehmann, P. and Or, D.: Evaporation from layered porous media, *J. Geophys. Res.*  
*Solid Earth*, 115(6), 1–12, doi:10.1029/2009JB006743, 2010.

1155 Shokri, N., P. Lehmann, P. Vontobel, and D. Or.: Drying front and water content dynamics  
during evaporation from sand delineated by neutron radiography. *Water resources research*,  
44(6), 2008.

Sillon, J. F., Richard, G. and Cousin, I.: Tillage and traffic effects on soil hydraulic properties and  
1160 evaporation, *Geoderma*, 116(1–2), 29–46, doi:10.1016/S0016-7061(03)00092-2, 2003.

Šimůnek, J., M. Šejna, A., Saito, H., Sakai, M. and Genuchten, M. T. Van: The HYDRUS-1D  
software package for simulating the movement of water, heat, and multiple solutes in variably  
saturated media, version 4.17, *HYDRUS Softw. Ser. 3D*, (June), 343, 2013.

1165

Soane, B. D. and van Ouwerkerk, C.: Implications of soil compaction in crop production for the  
quality of the environment, *Soil Tillage Res.*, 35(1–2), 5–22, doi:10.1016/0167-1987(95)00475-  
8, 1995.

1170 El Titi, A.: *Soil Tillage in Agroecosystems*, CRC Press, Boca Raton/London/New  
York/Washington D.C., 2003.

Wang, J.-P., Hu, N., Françoise, B. and Lambert, P.: Estimating water retention curves and  
strength properties of unsaturated sandy soils from basic soil gradation parameters, *Water*  
1175 *Resour. Res.*, 53, 6069–6088, doi:10.1002/2017WR020411. Received, 2017.

Weisbrod, N., Nachshon, U., Dragila, M. and Grader, A.: Micro-CT Analysis to Explore Salt  
Precipitation Impact on Porous Media Permeability, 231–241, doi:doi:10.1007/978-94-007-  
7534-3\_20, 2013.

1180

Yakirevich, A., Weisbrod, N., Kuznetsov, M., Rivera Villarreyes, C. A., Benavent, I., Chavez, A.  
M. and Ferrando, D.: Modeling the impact of solute recycling on groundwater salinization  
under irrigated lands: A study of the Alto Piura aquifer, Peru, *J. Hydrol.*, 482, 25–39,  
doi:10.1016/j.jhydrol.2012.12.029, 2013.

1185

Zhang, Y., Zhang, Z., Ma, Z., Chen, J., Akbar, J., Zhang, S., Cerdà, A., et al.: A review of preferential water flow in soil science. *Canadian Journal of Soil Science*. 98(4): 604-618., 2018.

1190 Zhou, T., J. Šimůnek, and I. Braud.: Adapting HYDRUS-1D to simulate the transport of soil water isotopes with evaporation fractionation. *Environmental Modelling & Software*, 143, 105118, 2021.